

Hybrid static potentials in SU(3) lattice gauge theory at small quark-antiquark separations

Carolin Schlosser¹ and Marc Wagner²

Goethe-Universität Frankfurt am Main, Institut für Theoretische Physik, Max-von-Laue-Straße 1, D-60438 Frankfurt am Main, Germany
and Helmholtz Research Academy Hesse for FAIR, Campus Riedberg, Max-von-Laue-Straße 12, D-60438 Frankfurt am Main, Germany



(Received 17 November 2021; accepted 14 February 2022; published 7 March 2022)

We compute the Π_u and Σ_u^- hybrid static potentials in SU(3) lattice gauge theory using four different lattice spacings ranging from $a = 0.040$ fm to $a = 0.093$ fm. We provide lattice data points for quark-antiquark separations as small as 0.08 fm, where the a -dependent self-energy as well as lattice discretization errors at tree level of perturbation theory and at leading order in a^2 have been removed. We also investigate and exclude possibly present systematic errors from topological freezing, due to the finite spatial lattice volume and from glueball decays. Moreover, we provide corresponding parametrizations of the potentials, which can e.g. be used for Born-Oppenheimer predictions of heavy hybrid mesons.

DOI: [10.1103/PhysRevD.105.054503](https://doi.org/10.1103/PhysRevD.105.054503)

I. INTRODUCTION

The constituent quark model is quite successful in explaining the properties of a variety of nonexotic hadrons, quark-antiquark pairs or triplets of quarks or antiquarks without gluonic excitations. However, a particular class of exotic mesons, so-called hybrid mesons, contain such gluonic excitations and, thus, cannot be studied in a proper way using the constituent quark model. These systems require approaches closer to QCD, which contain gluons as degrees of freedom. In this work we use lattice gauge theory and are interested in heavy hybrid mesons, which are composed of heavy c or b quarks and a surrounding excited gluon field. The gluonic excitation contributes to the quantum numbers of the hybrid meson such that exotic combinations of J^{PC} are allowed, which do not exist in the constituent quark model.

The experimental searches for exotic states in existing and future facilities such as the GlueX experiment at Jefferson Lab or the PANDA experiment at FAIR as well as the theoretical explanation of their internal structure and properties are currently hot research topics (for an experimental review see e.g. Ref. [1]; for theoretical reports we refer to Refs. [2–6]). Concerning theoretical approaches, lattice gauge theory is an ideal nonperturbative

first principles approach to investigate properties and masses of heavy hybrid mesons, either within the Born-Oppenheimer approximation [7–16] or in full lattice QCD (see e.g. Refs. [17–20]). We focus on hybrid mesons composed of heavy c or b quarks and use SU(3) lattice gauge theory in combination with the Born-Oppenheimer approximation [21], which is a two-step approach. In the first step, we fix the positions of the heavy quarks and compute so-called hybrid static potentials with lattice gauge theory. Hybrid static potentials correspond to energy levels of gluonic excitations in the presence of static quarks as functions of their separation. In the second step of the Born-Oppenheimer approximation, the radial Schrödinger equation for the relative coordinate of the heavy quark-antiquark pair is solved with one of the hybrid static potentials obtained in the first step.

In recent years a lot of effort was invested to refine the second step of the Born-Oppenheimer approximation, e.g. by including the mixing of different sectors via coupled channel equations [11–13] and by taking heavy quark spin effects into account [15,16]. These approaches require precise lattice results for hybrid static potentials, in particular at small quark-antiquark separations r to combine them with perturbative predictions valid only at small r or to fix matching coefficients in potential nonrelativistic QCD (pNRQCD) [12,15,16,22]. Thus, the main goal of this work is to use lattice gauge theory to investigate the small- r region of the Π_u and Σ_u^- hybrid static potentials. We aim at extending the range of precise lattice field theory results to smaller quark-antiquark separations and improve existing investigations of hybrid static potentials

Published by the American Physical Society under the terms of the Creative Commons Attribution 4.0 International license. Further distribution of this work must maintain attribution to the author(s) and the published article's title, journal citation, and DOI. Funded by SCOAP³.

[7–9,14,23–46]. For this we perform computations at four different lattice spacings ranging from $a = 0.040$ fm to $a = 0.093$ fm. These computations at several small lattice spacings do not only allow one to access smaller quark-antiquark separations than before, but also to explore and remove lattice discretization errors, such that our final results are expected to be consistent with the continuum limit within statistical errors. Moreover, we can convincingly confirm the repulsive behavior of hybrid static potentials at small r predicted by perturbation theory.

To compute the ordinary static potential and the Π_u and Σ_u^- hybrid static potentials we employ optimized operators from our previous work [14] as well as a multilevel algorithm [47]. In this way we obtain precise lattice results for these potentials on four ensembles for quark-antiquark separations as small as 0.08 fm (see Sec. II–IV). We also check that our lattice gauge theory computations are not contaminated by sizable systematic errors related to topological freezing, the finite spatial lattice volume or glueball decays of hybrid flux tubes, which are expected to be particularly prominent at small lattice spacings and small quark-antiquark separations (see Sec. VI). Moreover, we provide parametrizations describing the hybrid static potentials for quark-antiquark separations $0.08 \text{ fm} \lesssim r \lesssim 1.12 \text{ fm}$. We use these parametrizations to eliminate discretization errors and the a -dependent self-energy (see Sec. V). We also use the parametrizations to check the impact of including our new lattice data at small lattice spacings in Born-Oppenheimer predictions of $c\bar{c}$ and $b\bar{b}$ hybrid meson masses and find sizable differences from our previous work [14], where we have only considered a single lattice spacing $a = 0.093$ fm. The numerical values of all lattice data points and their parametrizations are provided for straightforward use in future applications, e.g. for predictions of heavy hybrid meson masses in more

refined Born-Oppenheimer approaches as proposed in Refs. [12,13,15,16]. We also provide similar results for gauge group $SU(2)$, which were obtained at an early stage of this work.

II. HYBRID STATIC POTENTIALS: QUANTUM NUMBERS, OPERATORS, AND CORRELATION FUNCTIONS

Hybrid static potentials represent the energy of the excited gluon field in the presence of a static quark and antiquark as a function of their separation.

Static potentials are characterized by the following three quantum numbers:

- (i) $\Lambda = \Sigma (= 0), \Pi (= 1), \Delta (= 2), \dots$, denotes the total angular momentum with respect to the quark-antiquark separation axis, i.e. is a non-negative integer (without loss of generality we separate the static quark and antiquark along the z axis).
- (ii) $\eta = g(=+), u(=-)$ describes the even (g) or odd (u) behavior under the combined parity and charge conjugation transformation $\mathcal{P} \circ \mathcal{C}$.
- (iii) $\epsilon = +, -$ is the eigenvalue of a reflection \mathcal{P}_x along an axis perpendicular to the quark-antiquark separation axis (for definiteness we use the x axis). For $\Lambda \geq 1$, hybrid static potentials are degenerate with respect to ϵ and ϵ is typically omitted.

The ordinary static potential has quantum numbers Σ_g^+ , while hybrid static potentials have quantum numbers different from Σ_g^+ . In this work we carry out a precise computation and parametrization of the two lowest hybrid static potentials, which have quantum numbers Π_u and Σ_u^- , with particular focus on rather small quark-antiquark separations r .

Hybrid static potentials are computed from correlation functions similar to Wilson loops, where the straight spatial parallel transporters are replaced by more complicated gauge link combinations with nontrivial transformation properties,

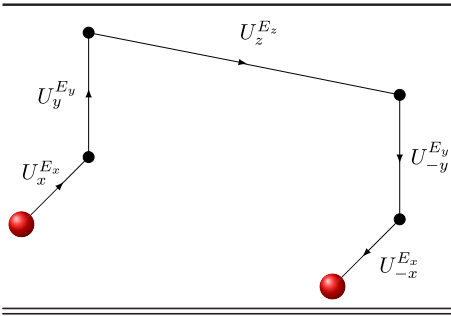
$$W_{S;\Lambda_\eta^\epsilon}(r, t) = \langle \text{Tr}(a_{S;\Lambda_\eta^\epsilon}(-r/2, +r/2; 0)U(+r/2; 0, t)(a_{S;\Lambda_\eta^\epsilon}(-r/2, +r/2; t))^\dagger U(-r/2; t, 0)) \rangle_U. \quad (1)$$

$U(r; t_1, t_2)$ is a straight path of temporal gauge links from time t_1 to time t_2 at spatial position $\mathbf{r} = (0, 0, r)$, and $\langle \dots \rangle_U$ denotes the average on an ensemble of gauge link configurations. $a_{S;\Lambda_\eta^\epsilon}$ is given by a sum of properly transformed spatial insertions USU , to probe the sector with quantum numbers Λ_η^ϵ ,

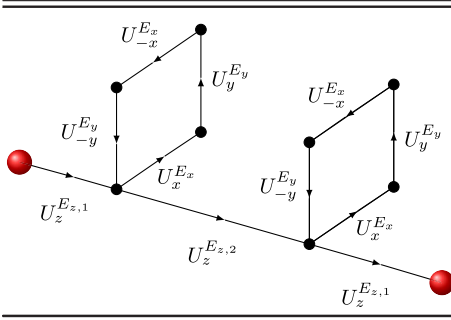
$$a_{S;\Lambda_\eta^\epsilon}(-r/2, +r/2) = \frac{1}{4} \sum_{k=0}^3 \exp\left(\frac{i\pi\Lambda k}{2}\right) R\left(\frac{\pi k}{2}\right) (U(-r/2, r_1)(S(r_1, r_2) + \epsilon S_{\mathcal{P}_x}(r_1, r_2))U(r_2, +r/2) \\ + U(-r/2, -r_2)(\eta S_{\mathcal{P} \circ \mathcal{C}}(-r_2, -r_1) + \eta \epsilon S_{(\mathcal{P} \circ \mathcal{C})\mathcal{P}_x}(-r_2, -r_1))U(-r_1, +r/2)). \quad (2)$$

The subscripts \mathcal{P}_x and $\mathcal{P} \circ \mathcal{C}$ denote the spatial reflection along the x axis and the charge conjugated reflection with respect to the origin. The notation is explained in detail in Ref. [14]. We employ operators S from Ref. [14], where we

have carried out a dedicated optimization to maximize the generated ground state overlaps. For the Π_u hybrid static potential we use $S_{\text{III},1}$ and for the Σ_u^- hybrid static potential we use $S_{\text{IV},2}$, which are defined and illustrated in Tables I

TABLE I. Optimized creation operator for V_{Π_u} [14].


$US_{\text{III},1}U = U_x^{E_x}U_y^{E_y}U_z^{E_z}U_{-y}^{E_y}U_{-x}^{E_x}$											
r/a	2	3	4	5	6	7	8	9	10	11	12
E_z	2	3	4	5	6	7	8	9	10	11	12
E_x	1	1	1	1	1	1	1	1	1	1	1
E_y	3	3	3	3	3	3	3	3	3	3	3

TABLE II. Optimized creation operator for $V_{\Sigma_u^-}$ [14].


$US_{\text{IV},2}U = U_z^{E_z,1}U_x^{E_x}U_y^{E_y}U_{-x}^{E_x}U_{-y}^{E_y}U_z^{E_z,2}U_x^{E_x}U_y^{E_y}U_{-x}^{E_x}U_{-y}^{E_y}U_z^{E_z,1}$											
r/a	2	3	4	5	6	7	8	9	10	11	12
$E_{z,1}$	0	0	0	1	1	2	2	3	3	4	4
$E_{z,2}$	2	3	4	3	4	3	4	3	4	3	4
E_x	3	3	3	3	3	3	3	3	3	3	3
E_y	3	3	3	3	3	3	3	3	3	3	3

and II. The spatial extents E_j listed in these tables in units of the lattice spacing a refer to and were optimized in Ref. [14] for $a = 0.093$ fm. For computations at smaller values of a we increase E_x and E_y such that they are approximately constant in physical units. See also the discussion in Appendix A.

To further enhance the ground state overlaps, we apply APE smearing (see e.g. Ref. [48] for detailed equations) to the spatial gauge links appearing in a_{S_i, Λ_i^c} . The number of APE smearing steps is increased with decreasing lattice spacing to keep the smearing radius approximately constant in physical units. Details can also be found in Appendix A.

III. COMPUTATIONAL DETAILS

A. Gauge link ensembles

We computed hybrid static potentials on both SU(2) and SU(3) gauge link configurations generated with the standard Wilson plaquette action without dynamical quarks. Results for purely gluonic observables such as energies in the presence of a static quark-antiquark pair, possibly in a sector with hybrid quantum numbers, are expected to be similar in pure gauge theory and in QCD (for hybrid static potentials this is supported by lattice results from Ref. [34]). To study hybrid static potentials, it might even be advantageous to use pure gauge theory, because in that case an excited flux tube can only decay into multiparticle states, which include rather heavy glueballs, but not light pions. In Sec. VIC glueball decays are discussed in detail.

In the main part of this work we focus exclusively on computations and results for gauge group SU(3). Corresponding results for gauge group SU(2) are summarized in Appendix E.

We generated four ensembles of gauge link configurations with gauge couplings $\beta = 6.594, 6.451, 6.284, 6.000$ using the CL2QCD software package [49]. We relate the corresponding lattice spacing a to the Sommer scale r_0 via a parametrization of $\ln(a/r_0)$ provided in Ref. [50], which is based on a precision determination of r_0 up to $\beta = 6.92$. We introduce physical units by setting $r_0 = 0.5$ fm, which is a simple and common choice in pure gauge theory, but is slightly larger than QCD results [51].

The details of our gauge link ensembles, which we label by $A, B, C,$ and D , are collected in Table III. The lattice volume for all four ensembles is $L^3 \times T \approx (1.2 \text{ fm})^3 \times 2.4 \text{ fm}$.¹ This is sufficiently large to neglect finite volume corrections (see Sec. VIB for a detailed investigation and discussion). Each ensemble was generated by N_{sim} independent Monte Carlo simulations, where each simulation comprises N_{total} updates. An update is composed of a heat-bath sweep and N_{or} overrelaxation sweeps. N_{or} is chosen roughly as $N_{\text{or}} \approx 1.5r_0/a$ following Ref. [53].

¹The ratio T/L is not exactly the same for the four ensembles. One reason for this is that the CL2QCD software package [49] requires an even number of lattice sites in both spatial and temporal directions. Moreover, ensembles C and D were generated previously for another project [52] and reused for our computation of hybrid static potentials.

TABLE III. Gauge link ensembles.

Ensemble	β	a in fm [50]	$(L/a)^3 \times T/a$	N_{sim}	N_{total}	N_{or}	N_{therm}	N_{sep}	N_{meas}
A	6.000	0.093	$12^3 \times 26$	2	60000	4	20000	50	1600
B	6.284	0.060	$20^3 \times 40$	2	60000	12	20000	100	800
C	6.451	0.048	$26^3 \times 50$	4	80000	15	40000	200	800
D	6.594	0.040	$30^3 \times 60$	4	80000	15	40000	200	800

This is expected to minimize correlations between subsequent gauge link configurations. The first N_{therm} updates are considered as thermalization updates and the corresponding gauge link configurations were, thus, discarded. After thermalization, gauge link configurations separated by N_{sep} updates were used to measure correlation functions, where N_{sep} is chosen significantly larger than the auto-correlation times of our observables. The total number of gauge link configurations used for measurements is thus $N_{\text{meas}} = N_{\text{sim}}(N_{\text{total}} - N_{\text{therm}})/N_{\text{sep}}$.

To eliminate autocorrelations, we combined these N_{meas} gauge link configurations into a much smaller number of bins. Statistical errors were determined using both the jackknife and the bootstrap methods. Further details concerning data analysis are discussed in Appendix B.

B. Multilevel algorithm

For the efficient computation of Wilson looplike correlation functions (1) we employ the multilevel algorithm [47]. The starting point for a multilevel simulation is one of the sets of N_{meas} thermalized gauge link configurations discussed in Sec. III A. The lattice is partitioned into n_{ts} time slices with thicknesses $p_1, p_2, \dots, p_{n_{\text{ts}}}$. In principle, time slices can be partitioned more than once, but we use only a single level of partitioning. For each time slice n_m sublattice configurations are generated using a standard heat-bath algorithm. These sublattice configurations are separated by n_u heat-bath sweeps, where links in the interior of the time slice are updated, while spatial links on the boundaries are fixed.

Two-link operators are defined via $\mathbb{T}(x, r\hat{j})_{\alpha\beta\gamma\delta} = U_0^*(x)_{\alpha\beta} U_0(x + r\hat{j})_{\gamma\delta}$ [\hat{j} denotes the spatial unit vector in the j -direction, e.g. $\hat{1} = (0, 1, 0, 0)$]. They are multiplied according to

$$\mathbb{P}_k = \{\mathbb{T}(x + (d_k - p_k)a\hat{0}, r\hat{j})\mathbb{T}(x + (d_k - p_k + 1)a\hat{0}, r\hat{j}) \cdots \mathbb{T}(x + (d_k - 1)a\hat{0}, r\hat{j})\} \quad (3)$$

with the multiplication prescription $\{\mathbb{T}_1\mathbb{T}_2\}_{\alpha\beta\gamma\delta} = \{\mathbb{T}_1\}_{\alpha\sigma\gamma\rho}\{\mathbb{T}_2\}_{\sigma\beta\rho\delta}$, such that the product \mathbb{P}_k connects the two boundaries of the time slice k , i.e. extends from $t/a = d_{k-1}$ to $t/a = d_k$ with $d_k = \sum_{j=1}^k p_j$. The products \mathbb{P}_k are then averaged over the n_m corresponding sublattice configurations with the results denoted as $[\mathbb{P}_k]$.

Wilson loops are computed via

$$W_{S;\Lambda_\eta^\epsilon}(r, t) = a_{S;\Lambda_\eta^\epsilon}(\mathbf{x}, \mathbf{x} + r\hat{j}; x_0)_{\alpha\gamma} \{[\mathbb{P}_k][\mathbb{P}_{k+1}] \cdots [\mathbb{P}_{k+n_t-1}]\}_{\alpha\beta\gamma\delta} (a_{S;\Lambda_\eta^\epsilon}(\mathbf{x}, \mathbf{x} + r\hat{j}; x_0 + t))_{\beta\delta}^*, \quad (4)$$

where the spatial parallel transporters $a_{S;\Lambda_\eta^\epsilon}$ [see Eq. (2)] are both located on boundaries between time slices. n_t denotes the number of time slices traversed by the Wilson loop, i.e. $d_{k-1} = x_0$ and $\sum_{j=1}^{n_t} p_{k+j} = t/a$. Finally, the samples $W_{S;\Lambda_\eta^\epsilon}(r, t)$ from Eq. (4) are averaged over spacetime, the three spatial directions, and the N_{meas} thermalized gauge link configurations.

Note that the time-slice partitioning might impose constraints on the temporal extent of Wilson loops, which can be computed. For simplicity we choose a regular pattern, where all time slices have thickness 2, i.e. $p_1 = p_2 = \dots = p_{n_{\text{ts}}} = 2$. This choice is not only simple but also efficient, because it allows one to exploit translational invariance in temporal direction extensively. Moreover, we use $n_m = 400$ and $n_u = 30$.

For a technically more detailed discussion of the multilevel algorithm see Sec. 3.2 of Ref. [52].

C. Tree-level improvement for static potentials

To reduce lattice discretization errors for the ordinary and for hybrid static potentials, we apply a tree-level improvement similar as in Ref. [54]. In the continuum in leading-order perturbation theory static potentials are proportional to $1/r$ due to one-gluon exchange. The ordinary static potential is attractive, while the Π_u and Σ_u^- hybrid static potentials exhibit a repulsive $1/r$ behavior, which is suppressed by the factor $1/8$. On an infinite spacetime lattice the leading order perturbative result can be computed in a straightforward way as discussed in Appendix C. The difference to its $1/r$ continuum counterpart represents lattice discretization errors at tree level. These discretization errors can be subtracted from the nonperturbative lattice data points obtained from Wilson looplike correlation functions (1). For this one needs to estimate the prefactor of the $1/r$ perturbative part, which is proportional to the strong coupling (see e.g. Ref. [55] and references therein). We do this in Sec. V with a suitable fit to the Σ_g^+ static potential.

We note that there is a related but slightly different method for tree-level improvement also common in the literature (see e.g. Refs. [50,55]). Instead of changing the lattice result for the value of the static potential at a given quark-antiquark separation, this separation is replaced by a so-called improved separation. According to our numerical tests this method works well for the static force. However, for static potentials it seems to be inferior to the method discussed in the previous paragraph, because of their linear behavior for large separations. We plan to discuss this in detail in another publication.

IV. LATTICE FIELD THEORY RESULTS FOR THE Π_u AND Σ_u^- HYBRID STATIC POTENTIALS

In the following we discuss our lattice field theory results $V_{\Lambda_\eta^\epsilon}^e(r)$ for static potentials with quantum numbers $\Lambda_\eta^\epsilon = \Sigma_g^+$ (the ordinary static potential) and $\Lambda_\eta^\epsilon = \Pi_u, \Sigma_u^-$ (the two lowest hybrid static potentials) for all four lattice ensembles $e \in \{A, B, C, D\}$ listed in Table III. They correspond to the ground state energies in the sectors with quantum numbers Λ_η^ϵ and quark-antiquark separation r .

To extract these static potentials, we compute temporal correlation functions $W_{\Lambda_\eta^\epsilon}^e(r, t)$ [see Eq. (1)] of suitably designed creation operators as discussed in Sec. II. We restrict the computations to temporal separations t , which are multiples of $2a$. This allows the use of a single multilevel time-slice partitioning, which is simple as well as efficient (for details see Sec. III B).

Effective potentials are defined in terms of the correlation functions $W_{\Lambda_\eta^\epsilon}^e(r, t)$ via

$$V_{\text{eff}; \Lambda_\eta^\epsilon}^e(r, t) = \frac{1}{2a} \ln \left(\frac{W_{\Lambda_\eta^\epsilon}^e(r, t)}{W_{\Lambda_\eta^\epsilon}^e(r, t+2a)} \right). \quad (5)$$

These effective potentials approach plateaus at large t , which correspond to the ground state energies, i.e.

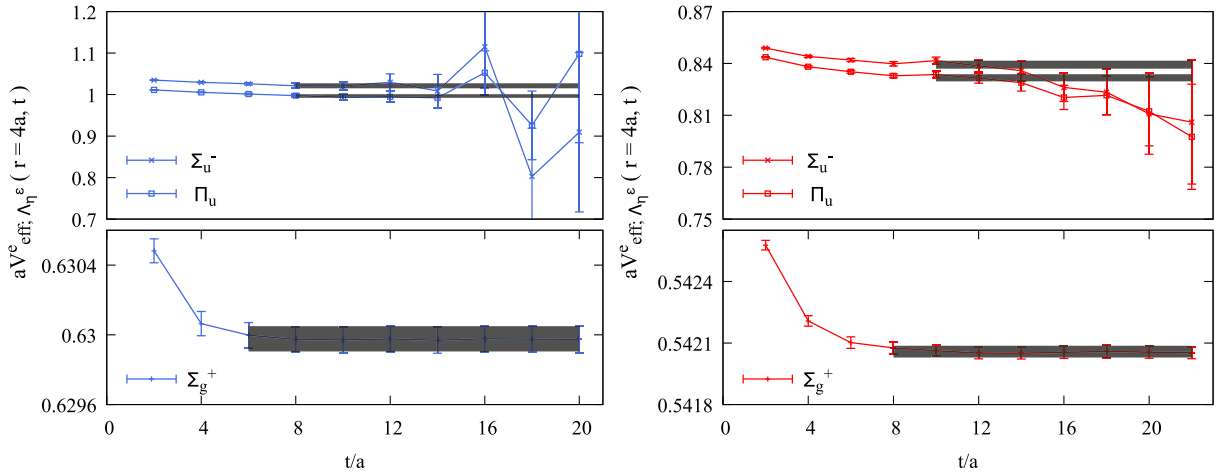


FIG. 1. Exemplary plots of effective potentials $aV_{\text{eff}; \Lambda_\eta^\epsilon}^e(r, t)$ with $\Lambda_\eta^\epsilon = \Sigma_g^+, \Pi_u, \Sigma_u^-$ for $r = 4a$ (Left: ensemble B, i.e. $a = 0.060$ fm; Right: ensemble D, i.e. $a = 0.040$ fm).

$$V_{\Lambda_\eta^\epsilon}^e(r) = \lim_{t \rightarrow \infty} V_{\text{eff}; \Lambda_\eta^\epsilon}^e(r, t). \quad (6)$$

Numerically the plateau values and, thus, the static potentials are extracted by uncorrelated χ^2 minimizing fits of constants to $aV_{\text{eff}; \Lambda_\eta^\epsilon}^e(r, t)$ in the range $t'_{\min} \leq t \leq t'_{\max}$. The fit range is chosen individually for each set of quantum numbers Λ_η^ϵ and each quark-antiquark separation r by an algorithm used already in our preceding work [14]:

- (i) t'_{\min} is defined as the minimal t , where the values of $aV_{\text{eff}; \Lambda_\eta^\epsilon}^e(r, t-2a)$ and $aV_{\text{eff}; \Lambda_\eta^\epsilon}^e(r, t)$ differ by less than 1σ .
- (ii) t'_{\max} is the maximal t , where $W_{\Lambda_\eta^\epsilon}^e(r, t+2a)$ has been computed, i.e. $t'_{\max} = 12a, 20a, 22a, 22a$ for ensembles A, B, C, D, respectively.
- (iii) Fits to $aV_{\text{eff}; \Lambda_\eta^\epsilon}^e(r, t)$ are performed for all ranges $t'_{\min} \leq t \leq t'_{\max}$ with $t_{\min} \leq t'_{\min}$, $t'_{\max} \leq t_{\max}$, and $t'_{\max} - t'_{\min} \geq 6a$.
- (iv) The result of the fit with the longest plateau and $\chi_{\text{red}}^2 \leq 1$ is taken as a result for $aV_{\Lambda_\eta^\epsilon}^e(r)$, where χ_{red}^2 is determined via

$$\chi_{\text{red}}^2 = \frac{2a}{t'_{\max} - t'_{\min}} \times \sum_{t=t'_{\min}, t'_{\min}+2a, \dots, t'_{\max}} \frac{(aV_{\text{eff}; \Lambda_\eta^\epsilon}^e(r, t) - aV_{\Lambda_\eta^\epsilon}^e(r))^2}{(\Delta aV_{\text{eff}; \Lambda_\eta^\epsilon}^e(r, t))^2} \quad (7)$$

with $\Delta aV_{\text{eff}; \Lambda_\eta^\epsilon}^e(r, t)$ denoting the statistical error of $aV_{\text{eff}; \Lambda_\eta^\epsilon}^e(r, t)$.

To confirm the validity of this procedure, we compared these results to results for $aV_{\Lambda_\eta^\epsilon}^e(r)$ obtained by fits in the range $t'_{\min} + 2a \leq t \leq t'_{\max}$. We found agreement within statistical errors. To illustrate the quality of our lattice data,

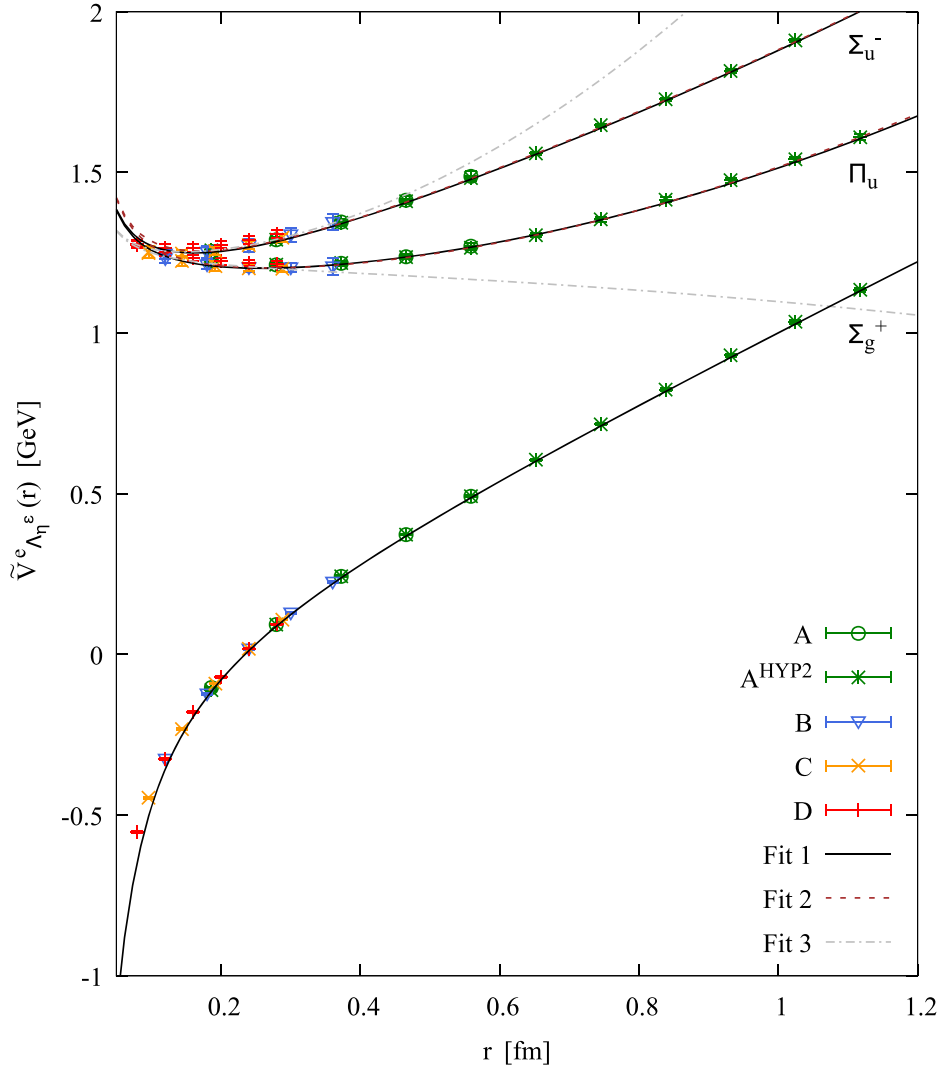


FIG. 2. Lattice data points $\tilde{V}_{\Lambda_\eta}^e(r)$ in GeV and corresponding parametrizations (9), (13), (14), and (15) as functions of the quark-antiquark separation r in fm. The colors green, blue, yellow, and red indicate different lattice spacings $a = 0.093$ fm, $a = 0.060$ fm, $a = 0.048$ fm, and $a = 0.040$ fm.

we show exemplary effective potential plots in Fig. 1. The final fit ranges $t'_{\min} \leq t \leq t'_{\max}$ and fit results are indicated by the horizontal lines.

The resulting static potentials $V_{\Lambda_\eta}^e(r)$ for $\Lambda_\eta^e = \Sigma_g^+, \Pi_u, \Sigma_u^-$ and separations $r \geq 2a$ are collected in units of the lattice spacing in Appendix D, Table VIII. Due to the regulator-dependent self-energy of static quarks, potentials computed at different lattice spacings a , i.e. on different ensembles e , are shifted relative to each other. We will subtract these self-energies in Sec. V, where we also remove discretization errors at tree level and partly proportional to a^2 , before we show the results for all ensembles together in a common plot in Fig. 2 and list them in physical units in Table IX.

Note that in contrast to previous lattice field theory computations of hybrid static potentials [7,8,14,26,27,29,36,40,41], where lattice spacings

$a \gtrsim 0.07$ fm were used,² our results are based on four ensembles with lattice spacings as small as 0.04 fm. Since lattice discretization errors in static potentials typically become large for $r \lesssim 2a$, the lattice potentials presented in this work are trustworthy down to $r \approx 0.08$ fm, whereas existing works were limited to separations roughly twice as large.

A major goal of this work is to explore the small- r region of the Π_u and Σ_u^- hybrid static potentials to make contact to perturbative calculations. Using the framework of

²In Ref. [27] hybrid static potentials were computed for gauge group SU(2) at very small lattice spacing $a \approx 0.022$ fm (when setting the scale as in Ref. [56]), but at the same time also at very small spatial volume, such that finite volume effects appear to be huge (see e.g. Fig. 1 in Ref. [27] and our detailed discussion of finite volume effects in Sec. VIB).

pNRQCD these hybrid static potentials have been predicted to be repulsive at very small r [12,13,40,57,58], a behavior that could not convincingly be confirmed by existing lattice computations because of the use of rather coarse lattice spacings. In contrast to that, our results from the ensembles with the fine lattice spacings $a \approx 0.048$ fm and $a \approx 0.040$ fm clearly show the predicted and expected upward curvature at small r (see Tables VIII and IX, and Fig. 2). This will be discussed in detail in Sec. V, where we parametrize our lattice data points by analytic functions based on pNRQCD predictions.

V. PARAMETRIZATION OF LATTICE RESULTS FOR HYBRID STATIC POTENTIALS

In this section we parametrize the lattice data points for the ordinary static potential $V_{\Sigma_g^+}(r)$ and the two lowest hybrid static potentials $V_{\Pi_u}(r)$ and $V_{\Sigma_u^-}(r)$ computed in Sec. IV and collected in Table VIII. The resulting parametrizations allow one to eliminate discretization errors to a large extent and can e.g. be used as input for Born-Oppenheimer predictions of heavy hybrid meson masses as previously done in Refs. [7–16].

In addition to the lattice data points specifically computed in the context of this work and discussed in Sec. IV, we use results from our previous computation [14] for quark-antiquark separations 0.19 fm $\lesssim r \lesssim 1.12$ fm to constrain our parametrizations also at large separations. This computation was performed at lattice spacing $a \approx 0.093$ fm, which is identical to the largest lattice spacing used in this work, i.e. to that of ensemble A. However, in contrast to the computations discussed in Sec. IV, HYP2 smeared temporal links [59–61] were used, which imply a significantly reduced self-energy and consequently smaller statistical errors, but possibly also larger discretization errors at small separations r . For completeness, these previous lattice results $V_{\Lambda_\eta^c}^{A^{\text{HYP2}}}(r)$ are also listed in Table VIII.

When combining the lattice results for the static potentials from the five ensembles $e \in \{A, B, C, D, A^{\text{HYP2}}\}$ (A^{HYP2} denotes the ensemble generated in the context of Ref. [14]), one needs to take into account that the self-energy is different for each ensemble. It depends on both the lattice spacing a and whether HYP2 smeared temporal links are used or not. To eliminate both the self-energy and lattice discretization errors at tree level, we first perform an eight-parameter uncorrelated χ^2 -minimizing fit of

$$V_{\Sigma_g^+}^{\text{fit},e}(r) = V_{\Sigma_g^+}(r) + C^e + \Delta V_{\Sigma_g^+}^{\text{lat},e}(r) \quad (8)$$

with the Cornell ansatz

$$V_{\Sigma_g^+}(r) = -\frac{\alpha}{r} + \sigma r \quad (9)$$

and

$$\Delta V_{\Sigma_g^+}^{\text{lat},e}(r) = \alpha' \left(\frac{1}{r} - \frac{G^e(r/a)}{a} \right) \quad (10)$$

to all lattice data points $V_{\Sigma_g^+}^e(r)$ with 0.2 fm $< r$. The fit parameters are the $1/r$ coefficient α , the string tension σ , the coefficient α' , and for each ensemble an additive constant C^e . The constants C^e absorb the ensemble dependent self-energies. $\Delta V_{\Sigma_g^+}^{\text{lat},e}(r)$ reflects lattice discretization errors at tree level, where the continuum result for the ordinary static potential at tree level is proportional to $1/r$ and its lattice counterpart $G^e(r/a)/a$ can be calculated numerically (see Refs. [50,54,62] and Appendix C). The physically meaningful part of the parametrization (8) is $V_{\Sigma_g^+}(r)$ with the two parameters α and σ . It is known that this Cornell ansatz provides an accurate description of the ordinary static potential for 0.2 fm $\lesssim r$ (see e.g. Ref. [63]). We note again that the ordinary static potential is only used to eliminate the self-energy and lattice discretization errors at tree level in the hybrid static potentials such that a precise parametrization of Σ_g^+ for $r < 0.2$ fm is not necessary.

The resulting fit parameters are collected in Table IV. In particular, we obtain $\alpha = 0.289(2) = 0.0571(4)$ GeV fm and $\sigma = 1.064(4)$ GeV/fm in reasonable agreement with results from the literature [64]. These fit parameters allow one to define data points

$$\tilde{V}_{\Sigma_g^+}^e(r) = V_{\Sigma_g^+}^e(r) - C^e - \Delta V_{\Sigma_g^+}^{\text{lat},e}(r), \quad (11)$$

where the self-energies and the lattice discretization errors at tree level are subtracted. These data points are collected in Table IX and plotted in Fig. 2. They are consistently parametrized by $V_{\Sigma_g^+}(r)$ for 0.2 fm $\leq r$ as demonstrated in the same figure.

Our parametrization of the Π_u and Σ_u^- hybrid static potentials is based on the pNRQCD prediction for small separations $r \ll 1/\Lambda_{\text{QCD}}$,

$$V_{\text{hybrid}}^{\text{pNRQCD}}(r) = V_o(r) + \Lambda_H + \mathcal{O}(r^2) \quad (12)$$

(see Refs. [12,57]). The pNRQCD hybrid static energies are given through the perturbative octet potential $V_o(r)$ and a nonperturbative constant Λ_H at leading order in a multipole expansion. The next term in such a multipole expansion is proportional to r^2 . At leading order in perturbation theory, $V_o(r) \propto 1/r$.

Simple fit functions consistent with this pNRQCD prediction are

$$V_{\Lambda_\eta^c}(r) = \frac{A_1}{r} + A_2 + A_3 \Lambda_\eta^c r^2, \quad (13)$$

where the parameters A_1 and A_2 are the same for both the Π_u and the Σ_u^- hybrid static potential, while the coefficients

TABLE IV. Resulting fit parameters. Fit 1 and Fit 2 correspond to the parametrizations (14) and (15) and fit ranges $2a \leq r$ and $3a \leq r$, respectively. Fit 3 corresponds to the parametrization (13) and fit range $2a \leq r \leq 0.3$ fm, where $A_{3,\Pi_u} = A_3$ and $A_{3,\Sigma_u^-} = A_3 + B_1$.

α [GeV fm]	σ [GeV/fm]		α' [GeV fm]		χ^2_{red}		
0.0571(4)	1.064(4)		0.0735(23)		0.7		
	A_1 [GeV fm]	A_2 [GeV]	A_3 [GeV fm ²]	B_1 [GeV fm ²]	B_2 [fm ⁻¹]	B_3 [fm ⁻²]	χ^2_{red}
Fit 1	0.0124(9)	1.135(8)	0.372(7)	1.56(15)	1.2(3)	2.1(2)	1.2
Fit 2	0.0147(18)	1.126(11)	0.381(7)	1.57(17)	1.0(4)	2.3(2)	0.8
Fit 3	0.0065(16)	1.190(14)	-0.092(91)	1.15(4)	-	-	0.5

Ensemble	C^e [GeV]	Fit 1		Fit 2		Fit 3		[GeV/fm ²]
		A'_{2,Π_u}	A'_{2,Σ_u^-}	A'_{2,Π_u}	A'_{2,Σ_u^-}	A'_{2,Π_u}	A'_{2,Σ_u^-}	
A	1.398(2)	3.1(7)	6.7(8)	3.0(9)	6.5(9)	3.4(8)	5.7(9)	
B	2.059(2)							
C	2.472(2)							
D	2.862(2)							
A ^{HYP2}	0.340(2)	1.0(7)	5.0(5)	0.9(9)	4.7(9)	1.6(7)	4.4(6)	

in front of the r^2 terms, A_{3,Π_u} and A_{3,Σ_u^-} , are independent. As in our preceding work [14], we found that Eq. (13) is suited to parametrize the Π_u potential in the r range, where lattice data points are available, but not suited to parametrize the Σ_u^- potential. Because of that we use extended fit functions already proposed in Ref. [14],

$$V_{\Pi_u}(r) = \frac{A_1}{r} + A_2 + A_3 r^2, \quad (14)$$

$$V_{\Sigma_u^-}(r) = \frac{A_1}{r} + A_2 + A_3 r^2 + \frac{B_1 r^2}{1 + B_2 r + B_3 r^2}, \quad (15)$$

which reduce to Eq. (13) in the limit of small separations.

Note that, in principle, all fit parameters depend on the lattice spacing a . In practice, however, only A_2 seems to have a sizable a dependence, as indicated by a small ensemble dependent additive offset particularly prominent at large a . We, thus, include the leading order lattice discretization error for A_2 , which is proportional to a^2 . It can be different for the Π_u and the Σ_u^- hybrid static potential and when using HYP2 smeared temporal links or not, i.e. is represented by terms $A'_{2,\Lambda_\eta^e} a^2$ with $A'_{2,\Pi_u}^A = A'_{2,\Pi_u}^B = A'_{2,\Pi_u}^C = A'_{2,\Pi_u}^D$ and $A'_{2,\Sigma_u^-}^A = A'_{2,\Sigma_u^-}^B = A'_{2,\Sigma_u^-}^C = A'_{2,\Sigma_u^-}^D$.

As previously for the ordinary static potential, we also include in the fit functions the constants C^e containing the self-energies. Moreover, we include a term reflecting discretization errors at tree level,

$$\Delta V_{\text{hybrid}}^{\text{lat},e}(r) = -\frac{1}{8} \Delta V_{\Sigma_\eta^+}^{\text{lat},e}(r) = -\frac{\alpha'}{8} \left(\frac{1}{r} - \frac{G^e(r/a)}{a} \right), \quad (16)$$

where the prefactor $-1/8$ relative to Eq. (10) is motivated by leading order perturbation theory. In summary, this amounts to a ten-parameter uncorrelated χ^2 minimizing fit of

$$V_{\Pi_u}^{\text{fit},e}(r) = V_{\Pi_u}(r) + C^e + \Delta V_{\text{hybrid}}^{\text{lat},e}(r) + A'_{2,\Pi_u} a^2, \quad (17)$$

$$V_{\Sigma_u^-}^{\text{fit},e}(r) = V_{\Sigma_u^-}(r) + C^e + \Delta V_{\text{hybrid}}^{\text{lat},e}(r) + A'_{2,\Sigma_u^-} a^2 \quad (18)$$

to the lattice data points $V_{\Pi_u}^e(r)$ and $V_{\Sigma_u^-}^e(r)$ of all five ensembles.

In Table IV we compare results obtained with two fit ranges, $2a \leq r$ (Fit 1) and $3a \leq r$ (Fit 2). In analogy to Eq. (11) we define data points

$$\tilde{V}_{\Lambda_\eta^e}^e(r) = V_{\Lambda_\eta^e}^e(r) - C^e - \Delta V_{\text{hybrid}}^{\text{lat},e}(r) - A'_{2,\Lambda_\eta^e} a^2, \quad (19)$$

where the self-energy as well as lattice discretization errors at tree level and proportional to a^2 in the difference from the ordinary static potential are removed. We note that data points $V_{\Lambda_\eta^e}^e(r) - C^e$, where only the ensemble dependent self-energy is subtracted, exhibit the expected linear behavior in a^2 caused by discretization errors. This is illustrated in Fig. 3, where $V_{\Sigma_\eta^+}^e(r) - C^e$ and $V_{\Pi_u}^e(r) - C^e$, $e = A, B, C, D$ are shown at fixed separation $r = 0.24$ fm as functions of the squared lattice spacing [for ensemble A there is no data point at $r = 0.24$ fm; we generated such a point by interpolating data points $V_{\Lambda_\eta^e}^A(r)$ close to $r = 0.24$ fm]. Linear extrapolations in a^2 to $a^2 = 0$ are consistent with the parametrizations (9) and (14) with parameters corresponding to Fit 1 as listed in Table IV

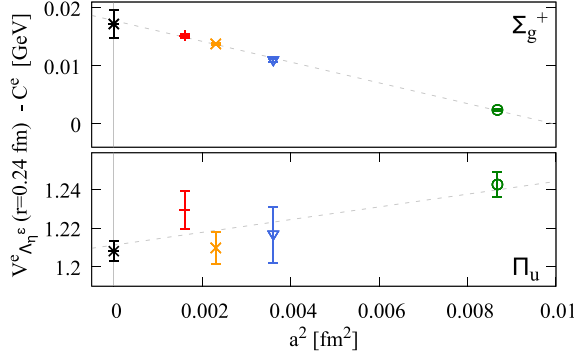


FIG. 3. Continuum extrapolations linear in a^2 using lattice data $V_{\Lambda_\eta^e}^e(r=0.24 \text{ fm}) - C^e$, $e = A, B, C, D$ for $\Lambda_\eta^e = \Sigma_g^+$ (top) and $\Lambda_\eta^e = \Pi_u$ (bottom). The results are consistent with the parametrizations (9) and (14) with parameters corresponding to Fit 1 as listed in Table IV (the black points).

(see again Fig. 3). This confirms that our strategy to eliminate discretization errors to a large extent in the parametrizations (9) and (14) is successful.

The data points defined in Eq. (19) are collected in Table IX and plotted in Fig. 2 together with the parametrizations (14) and (15). For larger separations, $r \gtrsim 0.2 \text{ fm}$, the parametrizations corresponding to $2a \leq r$ and to $3a \leq r$ are quite similar. For separations $r \lesssim 0.15 \text{ fm}$, however, there are clear deviations, which signal the importance of computing data points at small r . This is also reflected by the difference in the results for the coefficient A_1 of the repulsive $1/r$ term, $A_1 = 0.0124(9) \text{ GeV fm}$ versus $A_1 = 0.0147(18) \text{ GeV fm}$ for $2a \leq r$ and $3a \leq r$, respectively. Since the corresponding reduced χ^2 (listed in Table IV) indicate that both fits are of reasonable quality, we consider the parametrization obtained by taking into account a larger number of data points (i.e. Fit 1 with $2a \leq r$) to be superior and recommend to use this parametrization in future applications, e.g. Born-Oppenheimer predictions of heavy hybrid meson masses. A rather conservative strategy (which we do not follow in this work) would be to add a systematic error to the parametrization defined as the absolute difference between the parametrizations corresponding to Fit 1 and to Fit 2.

To study hybrid static potentials at small separations in even more detail, we performed an additional fit, where we fixed $B_2 = B_3 = 0$. The fit ansatz is then equivalent to Eq. (13), when identifying A_{3,Π_u} in Eq. (13) with A_3 in Eq. (14) and A_{3,Σ_u^-} in Eq. (13) with $A_3 + B_1$ in Eq. (15). Since the fit ansatz is then restricted to the perturbative prediction valid for small r , we use a reduced fit range, $2a \leq r \leq 0.3 \text{ fm}$. The fit is of reasonable quality, and as before the fit results are collected in Table IV and the corresponding parametrization is shown in Fig. 2. The coefficient of the repulsive $1/r$ term is now significantly smaller, $A_1 = 0.0065(16) \text{ GeV fm}$.

In summary, our lattice data points, for both the Π_u and the Σ_u^- hybrid static potential, clearly show a repulsive behavior at small separations, as predicted perturbatively in pNRQCD. We performed various fits with fit functions guided by these perturbative expansions, which are proportional to $1/r$ at small separations. We find the coefficient A_1 of the $1/r$ term in the region $0.005 \text{ GeV fm} \dots 0.017 \text{ GeV fm}$. A more precise determination of a parametrization of the repulsive region of hybrid static potentials will require further data points at even smaller separations and possibly refined fit functions with additional terms contributing to the small- r behavior.

Finally we compare to existing work, where the $1/r$ repulsion of the Π_u and the Σ_u^- hybrid static potentials was also quantified. In Ref. [65] the lattice data from Ref. [36] for the Π_u hybrid static potential was parametrized with a fit function similar to Eq. (13) with $A_1 = 0.022 \text{ GeV fm}$, which is larger than our results for A_1 from simultaneous fits to the Π_u and Σ_u^- potentials. Reference [13] follows the prediction from perturbation theory at leading order in α_s and fixes the $1/r$ -coefficient to $\alpha/8$, where α is obtained from a fit similar to Eq. (9) to lattice data from Ref. [36] in the range $0.2 \text{ fm} \leq r \leq 2.4 \text{ fm}$. The resulting $1/r$ -coefficient for the hybrid potentials is 0.012 GeV fm , which agrees with our fit results for the parameter A_1 for Fit 1 and Fit 2. In Ref. [12] hybrid static potential lattice data from Refs. [36,40] is parametrized consistently at small separations $0.08 \text{ fm} \leq r < 0.25 \text{ fm}$ by functions similar to Eq. (13). There, the $1/r$ -coefficient is not a fit parameter, but fixed to $\approx 0.01 \text{ GeV fm}$ by the perturbative octet potential calculated in the renormalon subtracted scheme up to order α_s^3 . This value for the $1/r$ -coefficient is in the ballpark of our fit results for A_1 .

A. Prediction of masses of heavy hybrid mesons

In the following we estimate masses of $\bar{c}c$ and $\bar{b}b$ hybrid mesons following the same Born-Oppenheimer approach as in our previous work [14], this time, however, using the refined and more accurate parametrizations (9), (14), and (15) with parameters corresponding to Fit 1 (see Table IV). Our goal is to quantify the impact of our new lattice data (results for ensembles A, B, C, and D), which cover smaller separations as well as several smaller lattice spacings than our previous data from ensemble A^{HYP2}.

We solve the radial Schrödinger equation

$$\left(-\frac{1}{2\mu} \frac{d^2}{dr^2} + \frac{L(L+1) - 2\Lambda^2 + J_{\Lambda_\eta^e}(J_{\Lambda_\eta^e} + 1)}{2\mu r^2} + V_{\Lambda_\eta^e}(r) \right) \times u_{\Lambda_\eta^e;L,n}(r) = E_{\Lambda_\eta^e;L,n} u_{\Lambda_\eta^e;L,n}(r), \quad (20)$$

using standard numerical techniques, i.e. a fourth order Runge-Kutta shooting method in combination with Newton's method for root finding. $\mu = m_{\bar{Q}}m_Q/(m_{\bar{Q}} + m_Q)$ is the reduced mass of the heavy $\bar{Q}Q$ pair, and we

TABLE V. Predictions for heavy hybrid meson masses.

Λ_η^ϵ	L	n	$m_{\Lambda_\eta^\epsilon;L,n}$ in GeV for $Q\bar{Q} = c\bar{c}$	$m_{\Lambda_\eta^\epsilon;L,n}$ in GeV for $Q\bar{Q} = b\bar{b}$
Π_u	1	1	4.175 (6)	10.682 (6)
	1	2	4.550 (8)	10.895 (6)
	2	1	4.360 (7)	10.785 (6)
	3	1	4.546 (8)	10.890 (7)
Σ_u^-	0	1	4.439 (5)	10.876 (5)
	0	2	4.878 (5)	11.153 (5)
	1	1	4.574 (5)	10.960 (5)
	1	2	5.001 (6)	11.228 (5)
	2	1	4.762 (5)	11.078 (5)
	3	1	4.964 (5)	11.205 (5)

use $m_c = 1628$ MeV and $m_b = 4977$ MeV from quark models [66]. For the potential $V_{\Lambda_\eta^\epsilon}(r)$ we employ our parametrizations (9), (14), or (15) with parameters listed as Fit 1 in Table IV. Following Ref. [11], we approximate the gluon spin $J_{\Lambda_\eta^\epsilon}$ by the gluon spin of a glue lump, i.e. $J_{\Sigma_g^+} = 0$ and $J_{\Lambda_\eta^\epsilon} = 1$ for $\Lambda_\eta^\epsilon = \Pi_u, \Sigma_u^-$. This approximation is motivated by the limit $r \rightarrow 0$, where the gluon configuration of a state representing a hybrid static potential becomes identical to that of the corresponding glue lump. $\psi_{\Lambda_\eta^\epsilon;L,n,m_L}(r, \theta, \phi) = (u_{\Lambda_\eta^\epsilon;L,n}(r)/r)Y_{L,m_L}(\theta, \phi)$ is the wave function of the relative coordinate of the quark-antiquark pair with $L \in \{\Lambda, \Lambda + 1, \dots\}$ denoting the orbital angular momentum of the $Q\bar{Q}$ pair of the hybrid meson. For details on the interpretation of the resulting energy levels and their assignment to hybrid meson multiplets we refer to Ref. [14].

In Table V we provide our updated results for heavy hybrid meson masses, which are defined according to

$$m_{\Lambda_\eta^\epsilon;L,n} = E_{\Lambda_\eta^\epsilon;L,n} - E_{\Lambda_\eta^\epsilon; \Sigma_g^+; n=1, L=0} + \bar{m}, \quad (21)$$

where $E_{\Lambda_\eta^\epsilon; \Sigma_g^+; n=1, L=0}$ is the lowest energy level computed with the ordinary static potential and \bar{m} is the corresponding spin averaged mass of the lightest quarkonium from experiments, either $\bar{m} = (m_{\eta_c(1S), \text{exp}} + 3m_{J/\Psi(1S), \text{exp}})/4 = 3.069(1)$ GeV or $\bar{m} = (m_{\eta_b(1S), \text{exp}} + 3m_{\Upsilon(1S), \text{exp}})/4 = 9.445(1)$ GeV [67]. In particular, the masses obtained with $V_{\Sigma_u^-}(r)$ are around 55 MeV lower for $c\bar{c}$ and 35 MeV lower for $b\bar{b}$ compared to our previous results from Ref. [14]. The masses related to $V_{\Pi_u}(r)$ are around 20 MeV lower for $c\bar{c}$ and almost unchanged for $b\bar{b}$. These discrepancies are similar to our newly introduced term $A_{2, \Lambda_\eta^\epsilon}^{\prime e} a^2$ evaluated for $e = A^{\text{HYP2}}$, which is 43(4) MeV for $\Lambda_\eta^\epsilon = \Sigma_u^-$ and 9(6) MeV for $\Lambda_\eta^\epsilon = \Pi_u$. The term $A_{2, \Lambda_\eta^\epsilon}^{\prime e} a^2$ represents lattice discretization errors, and can be determined only when static potential lattice data are available for several lattice spacings. This demonstrates that the lattice data and the corresponding parametrizations provided in this work

constitute an important step toward higher precision in Born-Oppenheimer predictions of heavy hybrid meson masses. The remaining discrepancies seem to be mostly related to the coefficient α in the parametrization (9) of $V_{\Sigma_g^+}(r)$, for which we quoted $\alpha = 0.0518(5)$ GeV fm in Ref. [14] and which we updated to $\alpha = 0.0571(4)$ GeV fm in this work. This change in α might also be a consequence of our careful identification and removal of lattice discretization errors, this time related to the tree-level improvement represented by the term $\Delta V_{\Sigma_g^+}^{\text{lat}, e}(r)$ defined in Eq. (10).

We note that our prediction of heavy hybrid meson masses within the Born-Oppenheimer approximation is based on several limiting assumptions (see the discussion in Sec. 6.2 in Ref. [14]), e.g. the single-channel approximation, where mixing between static potentials is excluded, and the neglect of effects due to the heavy quark spins. More sophisticated coupled channel Schrödinger equations were derived and used for Born-Oppenheimer predictions in Refs. [12,13]. Moreover, in Refs. [15,16] first steps were taken to include corrections from the heavy quark spins. These more advanced approaches also require lattice field theory results for the ordinary static potential and the Π_u and Σ_u^- hybrid static potentials. However, the corresponding predictions of heavy hybrid meson masses are based on lattice field theory results obtained at significantly larger lattice spacing than our smallest lattice spacing and corresponding parametrizations trustworthy only at larger quark-antiquark separations and presumably suffering from sizable lattice discretization errors. It would be interesting to repeat the Born-Oppenheimer computations from Refs. [12,13,15,16] with the lattice field theory results for static potentials from this work provided in Table IX.

Finally we note that a precision determination of heavy hybrid meson masses in a Born-Oppenheimer framework also requires precise knowledge of static potentials for separations even smaller than 0.08 fm, for which lattice computations were carried out in this work. In this small- r region higher order perturbation theory might be more suited than lattice QCD. In Ref. [63] the combination of next-to-next-to-next-to leading order (NNNLO) perturbation theory and lattice QCD is discussed for the Σ_g^+ potential. It would be worthwhile to advance in the same direction for hybrid static potentials.

VI. EXCLUDING SYSTEMATIC ERRORS

A. Topological freezing

In the continuum, gauge field configurations can be classified according to their integer topological charge Q . The corresponding topological sectors are separated by barriers of infinite action.

Topological freezing refers to the problem that a Monte Carlo simulation of a lattice gauge theory is trapped in one of the topological sectors, either during a significant part or the whole simulation. Clearly, gauge link

configurations generated in such a simulation do not form a representative set distributed according to e^{-S} . Topological freezing is expected to appear when using small lattice spacings $a \approx 0.05$ fm [68]. It becomes increasingly more problematic when approaching the continuum, i.e. when further decreasing a . If a simulation is fully trapped in a topological sector, observables exhibit specific finite volume corrections proportional to powers of $1/V$ (V denotes the spacetime volume) [69–72] in addition to finite volume corrections not related to topological freezing, which are discussed in Sec. VI B.

Since our lattice spacings are as small as 0.04 fm, we consider it important and necessary to check and compare the Monte Carlo histories of the topological charge for all our simulations. We use a field strength definition of the topological charge on the lattice (for a discussion and comparison of various definitions see Refs. [73,74])

$$Q = a^4 \sum_x q(x) \quad (22)$$

with the clover-leaf discretization of the topological charge density

$$q(x) = \frac{1}{32\pi^2} \sum_{\mu,\nu,\sigma,\rho=0}^3 \epsilon_{\mu\nu\rho\sigma} \text{Tr}(C_{\mu\nu}^{\text{clov}}(x) C_{\rho\sigma}^{\text{clov}}(x)), \quad (23)$$

$$C_{\mu\nu}^{\text{clov}}(x) = \frac{1}{4} \mathfrak{S}(P_{\mu\nu}(x) + P_{\nu-\mu}(x) + P_{-\mu-\nu}(x) + P_{-\nu\mu}(x)). \quad (24)$$

To eliminate UV fluctuations, which do not contribute to the topological charge, but might cause strong distortions of the corresponding lattice results, a smoothing procedure needs to be applied to the gauge links. We use four-dimensional APE smearing, similar to the three-dimensional APE smearing for the static potential operators, with $\alpha_{\text{APE}} = 0.3$. The number of smearing steps is chosen individually for each lattice spacing. We stop smearing as soon as Q is stable for several smearing steps for the majority of gauge link configurations. We computed the topological charge on all gauge link configurations of the four ensembles *A*, *B*, *C*, and *D* given in Table III. In Fig. 4(a) we show exemplarily the Monte Carlo histories of the topological charge for a subset of gauge link configurations for ensemble *B* ($a = 0.06$ fm) and

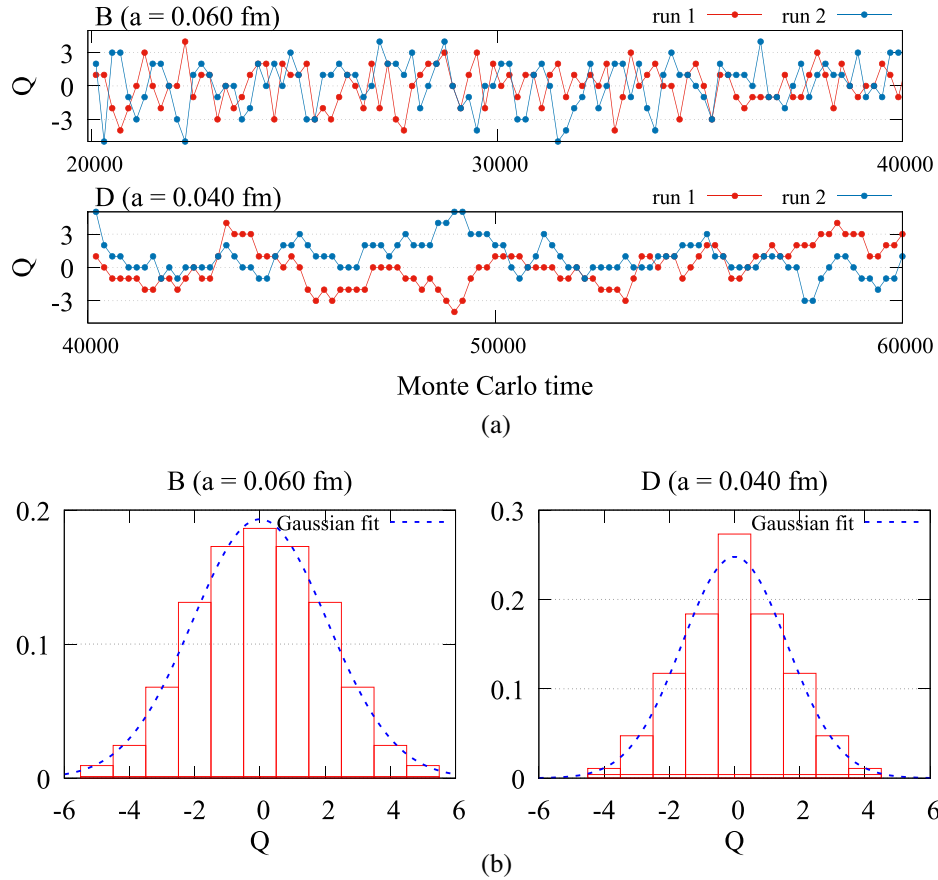


FIG. 4. (a) Monte Carlo histories of the topological charge for ensemble *B* ($a = 0.06$ fm) and *D* ($a = 0.04$ fm) for two independent simulation runs. (b) Normalized and symmetrized histograms reflecting the topological charge distribution for ensemble *B* and ensemble *D*.

D ($a = 0.04$ fm). At $a = 0.06$ fm the topological charge changes frequently and topological freezing is clearly not a problem. At $a = 0.04$ fm the autocorrelation time of Q is much longer, consistent with the expectation from Ref. [68]. However, there are still sufficiently many changes, such that our statistical error analysis, based on four independent simulation runs and a suitable binning (see Appendix B), should provide realistic uncertainties for the static potentials.

In Fig. 4(b) we show normalized and symmetrized histograms reflecting the topological charge distribution for ensembles B and D . Both are consistent with Gaussian distributions, as expected at finite, large spacetime volume. From their squared widths, $\langle Q^2 \rangle$, we obtain estimates of the related topological susceptibilities via $\chi_{\text{top}} = \langle Q^2 \rangle / V$, which are in reasonable agreement with results from the literature [75]. This is another indication that our computations of static potentials do not suffer from the problem of topological freezing.

B. Finite volume corrections

All static potential results discussed in Secs. IV and V were obtained from simulations with periodic spatial volume $L^3 \approx (1.2 \text{ fm})^3$. Since this is a rather small volume, it is important to check that finite volume corrections to these results are negligible.

One source of finite volume corrections is that of virtual glueballs traveling around the far side of the periodic spacetime volume. They cause a negative shift of energy levels, which is proportional to $\exp(-m_{0^{++}}L)$ at asymptotically large L [76] ($m_{0^{++}}$ denotes the mass of the lightest glueball). Note that in pure gauge theory such finite volume corrections are much more strongly suppressed than e.g. in QCD, where the lightest particles are pions with a mass much smaller than that of the 0^{++} glueball. We observe a small negative shift for the ordinary static potential for $L \ll 1.0$ fm, which could be related to such glueball interactions. Another type of finite volume correction will appear when the (infinite volume) wave function of a state has a larger extent than the finite spacetime volume of the

lattice. Then this wave function is necessarily squeezed, which will lead to a positive shift of the corresponding energy level [77]. For the Π_u and Σ_u^- hybrid static potentials we found sizable positive shifts for $L \ll 1.0$ fm. Since their wave functions cover a significantly larger region than the ordinary static potential [78], these positive shifts are also consistent with expectation.

In Fig. 5(a) we show the difference between the Π_u hybrid static potential and the ordinary static potential, $V_{\Pi_u} - V_{\Sigma_g^+}$, at fixed quark-antiquark separation $r = 0.25$ fm as a function of the spatial lattice extent L for gauge group SU(2). This difference is consistent with a constant, i.e. L -independent, for $L \gtrsim 1.0$ fm. For smaller L , however, the difference increases, which is consistent with the previously discussed expectation of a squeezed wave function for the Π_u hybrid static potential.

Additionally, for gauge group SU(3) we compared results for the Σ_g^+ , the Π_u , and the Σ_u^- static potential from ensemble A to results from an analogous computation with approximately twice the spatial lattice extent, i.e. $L = 2.4$ fm. We did not find statistically significant differences, as can be seen in Fig. 5(b). In summary, the investigations and checks discussed in this subsection strongly indicate that finite volume corrections at our preferred spacetime volume $L^3 \times T \approx (1.2 \text{ fm})^3 \times 2.4 \text{ fm}$ are small compared to current statistical errors and, thus, can be neglected.

C. Glueball decay

At sufficiently small r , the energy difference between a hybrid static potential and the ordinary static potential is large enough such that the Λ_η^c hybrid flux tube can decay into a glueball and the Σ_g^+ ground state. The threshold energy for a decay into the lightest glueball with quantum numbers $J^{PC} = 0^{++}$ and mass $m_{0^{++}} = 1.73(5)$ GeV [79] is shown as a dashed line in Fig. 6 together with lattice results for hybrid static potentials from Ref. [14]. The critical separations $r_{\text{crit}}^{\Lambda_\eta^c}$, where the dashed line intersects the Λ_η^c hybrid static potentials, are listed in Table VI. For $r \leq r_{\text{crit}}^{\Lambda_\eta^c}$ decays to a 0^{++} glueball are energetically allowed.

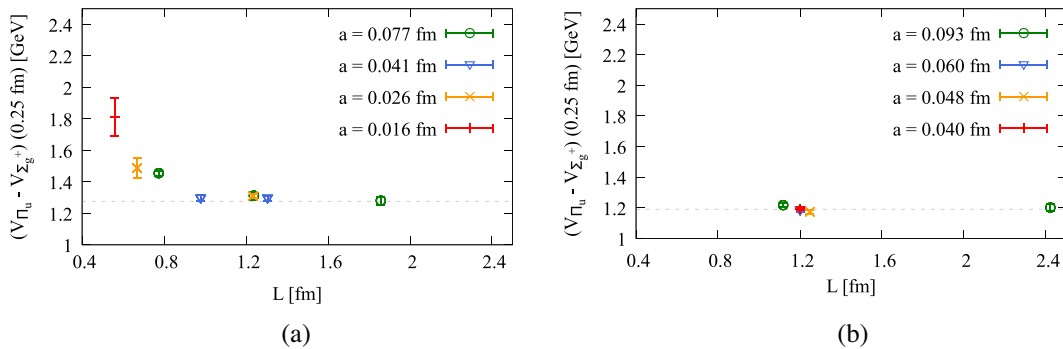


FIG. 5. $V_{\Pi_u}(0.25 \text{ fm}) - V_{\Sigma_g^+}(0.25 \text{ fm})$ as a function of the spatial lattice extent L for gauge groups SU(2) and SU(3). (a) SU(2) and (b) SU(3).

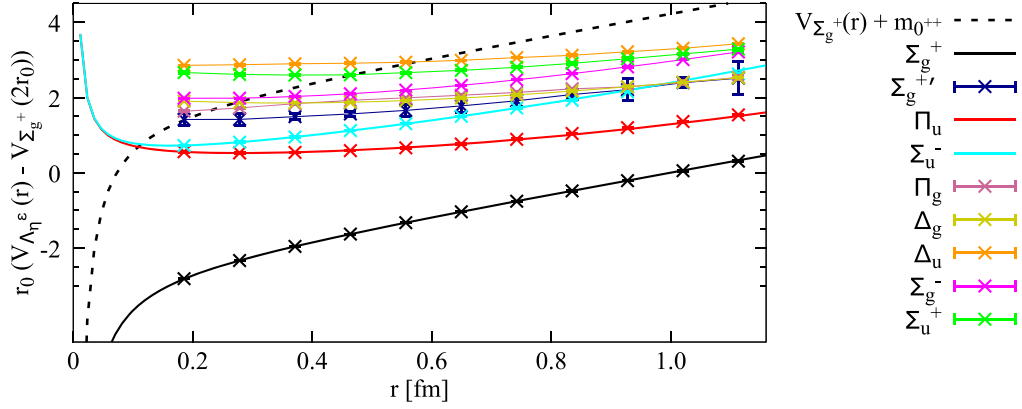


FIG. 6. Threshold energy for decays of hybrid flux tubes into the Σ_g^+ ground state and a 0^{++} glueball (dashed line) and hybrid static potentials for various quantum numbers Λ_η^ϵ . Static potentials are taken from Ref. [14], the 0^{++} glueball mass from Ref. [79].

However, such decays might be excluded because of quantum numbers. A comprehensive and general derivation of selection rules for both hybrids and tetraquarks can be found in Ref. [2]. Here we focus on hybrid static potentials with quantum numbers Λ_η^ϵ and discuss whether decays to the Σ_g^+ ground state and a $J^{PC} = 0^{++}$ glueball are possible. Since $J = 0$ for the considered glueball, also $J_z = 0$. Thus, the z -component of the orbital angular momentum of the glueball must be $L_z = \Lambda$ (as stated in Sec. II, the static quark and antiquark are separated along the z axis). The quantum number η does not protect a hybrid flux tube because the distribution of the glueball in the z -direction can be symmetric or antisymmetric. There is, however, a constraint due to the quantum number ϵ . The 0^{++} glueball is symmetric with respect to \mathcal{P}_x . Its orbital angular momentum wave function is also symmetric with respect to \mathcal{P}_x for $L_z = \Lambda = \Sigma = 0$. For $L_z = \Lambda > 0$ there are two independent possibilities for the wave function, one of them symmetric, the other antisymmetric. From this one can conclude that a 0^{++} glueball decay is not possible for Σ_u^- and for Σ_g^- , while it is allowed for all other hybrid flux tubes.

Decays into heavier glueballs with quantum numbers J^{PC} different from 0^{++} (some of them are antisymmetric with respect to \mathcal{P}_x) are energetically only allowed for separations much smaller than those listed in Table VI. Thus, they are not relevant in the context of our work.

In Secs. IV and V we presented and used lattice results for separations as small as $r \approx 0.08$ fm. Since $r_{\text{crit}}^{\Pi_u} = 0.11$ fm, results for the Π_u hybrid static potential

TABLE VI. Maximal separation $r_{\text{crit}}^{\Lambda_\eta^\epsilon}$, where a decay of a Λ_η^ϵ hybrid flux tube into the Σ_g^+ ground state and a 0^{++} glueball is energetically possible. For Σ_u^- and Σ_g^- such decays are excluded because of quantum numbers.

Λ_η^ϵ	Π_u	Π_g	Δ_g	Δ_u	$\Sigma_g^{+'}$	Σ_u^+	Σ_u^-	Σ_g^-
$r_{\text{crit}}^{\Lambda_\eta^\epsilon}$ [fm]	0.11	0.23	0.28	0.58	0.19	0.46	0.11	0.3

below that separation might be contaminated by a “ $\Sigma_g^+ + \text{glueball}$ ” scattering state. However, we observe the expected upward curvature for the Π_u hybrid static potential (see Fig. 2). Moreover, the Π_u and Σ_u^- hybrid static potentials approach each other for small r , consistent with the expected degeneracy in the limit $r \rightarrow 0$. Thus, we conclude that a possible contamination of our results for the Π_u hybrid static potential is negligible compared to statistical errors.

VII. SUMMARY AND OUTLOOK

We computed the ordinary static potential and the Π_u and Σ_u^- hybrid static potentials in SU(3) lattice gauge theory at four different lattice spacings, where the smallest lattice spacing, $a = 0.04$ fm, is roughly half the size of lattice spacings previously used in similar computations. Lattice discretization errors, which were found to be sizable in the bare lattice data points, were studied in detail. We removed a large part of these discretization errors by using both perturbative tree-level improvement and a suitable simultaneous fit to the bare lattice data points from all our ensembles to identify the dominant a^2 contribution to the discretization errors. Using the same fit we were also able to subtract the a -dependent unphysical self-energy. For future reference these improved lattice data points are collected in Table IX. Moreover, we investigated possibly existent systematic errors related to topological freezing, due to the finite spatial volume and because of glueball decays in detail and provided evidence that these errors are negligible compared to statistical errors.

We also provide parametrizations of the Σ_g^+ , Π_u , and Σ_u^- static potentials, which can e.g. be used for Born-Oppenheimer predictions of heavy hybrid meson masses. The Born-Oppenheimer approach in the context of heavy hybrid mesons received considerable interest in the past couple of years, with many improvements and refinements, e.g. the derivation of coupled channel Schrödinger equations, which take into account mixing between different

sectors [12,13], or the inclusion of effects due to the heavy quark spins [15,16]. These papers, however, use lattice data [8,29,33,36,40,41] generated around two decades ago at much coarser lattice spacing and partly without any dedicated investigation or removal of discretization errors. Thus, it would be an interesting and important step toward higher precision to combine the refined Born-Oppenheimer approaches from Refs. [12,13,15,16] with the lattice data points or the parametrizations presented in this work.

Since we performed computations at very small lattice spacings, we were able to reliably access quark-antiquark separations as small as $r = 0.08$ fm. This, in turn, allowed us to convincingly show the upward curvature at small r of the Π_u and Σ_u^- hybrid static potentials predicted by perturbation theory, i.e. their repulsive nature at small quark-antiquark separations. An interesting future direction with the aim to improve the precision of Born-Oppenheimer predictions even further could be to match higher order perturbation theory and the lattice results presented in this work. For the ordinary static potential a possible method using next-to-next-to-next-to-leading order perturbation theory was discussed in Ref. [63] and an approach based on leading order perturbation theory for hybrid static potentials can be found in Ref. [12].

ACKNOWLEDGMENTS

We thank Christian Reisinger for providing his multi-level code. We acknowledge interesting and useful discussions with Eric Braaten, Nora Brambilla, Francesco Knechtli, Colin Morningstar, Lasse Müller, Christian Reisinger, and Joan Soto. M. W. acknowledges support by the Heisenberg Programme of the Deutsche Forschungsgemeinschaft (DFG, German Research Foundation)—Project No. 399217702. Calculations on the GOETHE-HLR and on the FUCHS-CSC high-performance computers of the Frankfurt University were conducted for this research. We thank HPC-Hessen, funded by the State Ministry of Higher Education, Research and the Arts, for programming advice.

APPENDIX A: OPTIMIZATION OF OPERATORS

The operators S appearing in Eq. (2) were optimized in Ref. [14] at lattice spacing $a = 0.093$ fm with respect to their generated ground state overlaps. This was done by minimizing the effective potential at small temporal separation $t = a$ with respect to the operator extents E_j defined in Tables I and II. To crudely retain this optimization also for smaller values of the lattice spacing without investing additional computer resources, we adjust the operator extents E_x and E_y in units of the lattice spacing (which are restricted to integers) such that their values in physical units are approximately independent of a . We tested this procedure numerically for $S_{\text{III},1}$ and gauge group SU(2) and found satisfactory ground state overlaps also for rather

TABLE VII. Smearing parameter N_{APE} for various lattice spacings for gauge groups SU(2) and SU(3).

a in fm	0.078	0.041	0.026	
N_{APE} for SU(2)	30	100	200	
a in fm	0.093	0.060	0.048	0.040
N_{APE} for SU(3)	20	50	75	100

small values of the lattice spacing. Moreover, we select N_{APE} , the number of APE-smearing steps, individually for each lattice spacing, while keeping $\alpha_{\text{APE}} = 0.5$ constant (see e.g. Ref. [48] for detailed equations). We do this in such a way that the effective potentials of the Π_u and the Σ_u^- hybrid static potentials at temporal separation $t/a = 2$ are small. This amounts to increasing N_{APE} for decreasing a . Our preferred values for N_{APE} for both gauge groups SU(2) and SU(3) are listed in Table VII.

APPENDIX B: ERROR ANALYSIS

To eliminate correlations in Monte Carlo time, we combine consecutively generated gauge link configurations, which are used for the computation of static potentials, to N^e bins.

For the data points $V_{\Lambda_\eta^c}^e(r)$ (see Sec. IV) statistical errors are determined via a standard jackknife analysis, i.e. from N^e reduced jackknife samples $V_{\Lambda_\eta^c,j}^{e,\text{jackknife}}(r)$ according to

$$\Delta V_{\Lambda_\eta^c}^e(r) = \left(\frac{N^e - 1}{N^e} \sum_{j=1}^{N^e} (V_{\Lambda_\eta^c,j}^{e,\text{jackknife}}(r) - \bar{V}_{\Lambda_\eta^c}^e(r))^2 \right)^{1/2} \quad (\text{B1})$$

[$\bar{V}_{\Lambda_\eta^c}^e(r)$ denotes the result for the full sample].

The fits from Sec. V, where data points of all five ensembles are used at the same time, can in principle also be computed via the jackknife method. The number of reduced jackknife samples, however, would be rather large, $N^A \times N^B \times N^C \times N^D \times N^{A^{\text{HYP}2}}$, and the corresponding computational effort huge. Therefore, we use for these fits and all following analyses the bootstrap method. To this end we first inflate the reduced jackknife samples,

$$V_{\Lambda_\eta^c,j}^e(r) = \bar{V}_{\Lambda_\eta^c}^e(r) + (N^e - 1)(V_{\Lambda_\eta^c,j}^{e,\text{jackknife}}(r) - \bar{V}_{\Lambda_\eta^c}^e(r)). \quad (\text{B2})$$

A bootstrap sample is then generated by randomly selecting N^e of the inflated samples $V_{\Lambda_\eta^c,j}^e(r)$ for each ensemble, where the same inflated sample may be selected more than once. As usual, the bootstrap error of a quantity O is then the standard deviation of the results obtained on the bootstrap samples, i.e.

$$\Delta O = \left(\frac{1}{K} \sum_{j=1}^K (O_j - \bar{O})^2 \right)^{1/2}. \quad (\text{B3})$$

O_j denotes the result on the j th bootstrap sample and \bar{O} the result on the full sample, where O can be α , σ , α' , C^e , A_1 , A_2 , etc. K , the number of bootstrap samples, has to be chosen sufficiently large, such that ΔO is essentially independent of K .

For our computations we used $N^A = 320$, $N^B = N^C = N^D = 160$, $N^{A^{\text{HYP2}}} = 5000$, and $K = 10000$.

APPENDIX C: TREE-LEVEL IMPROVEMENT

In the continuum at tree level of perturbation theory the ordinary static potential is attractive and proportional to

$$G^{\text{HYP}}(\mathbf{R}) = \frac{1}{(2\pi)^3} \int_{-\pi}^{\pi} d^3k \frac{\prod_{j=1}^3 \cos(k_j R_j) \times (1 - (\alpha_1/6) \sum_{i=1}^3 4\sin^2(k_i) \Omega_{i0})^2}{4 \sum_{j=1}^3 \sin^2(k_j/2)}, \quad (\text{C2})$$

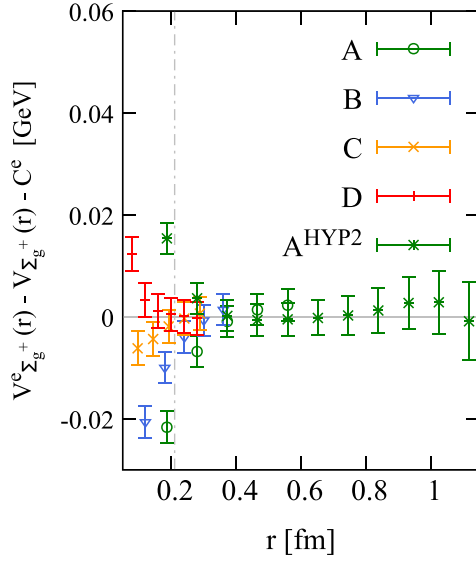
where $\Omega_{\mu\nu}$ is

$$\Omega_{\mu\nu} = 1 + \alpha_2(1 + \alpha_3) - \frac{\alpha_2}{4}(1 + 2\alpha_3) \left(\sum_{j=1}^3 4\sin^2(p_j/2) - 4\sin^2(p_\mu/2) - 4\sin^2(p_\nu/2) \right) + \frac{\alpha_2\alpha_3}{4} \prod_{\eta \neq \mu, \nu} 4\sin^2(p_\eta/2) \quad (\text{C4})$$

(see Ref. [54]). This integral can be solved e.g. by standard Monte Carlo integration techniques.

To eliminate lattice discretization errors at tree level for the ordinary static potential, we subtract

$$\Delta V_{\Sigma_g^+}^{\text{lat},e}(r) = \alpha' \left(\frac{1}{r} - \frac{G^e(r/a)}{a} \right) \quad (\text{C5})$$



$1/r$. Its lattice counterpart for the standard Wilson plaquette gauge action and the Eichten-Hill static action is

$$\left(\frac{1}{r} \right)_{\text{lat}} = 4\pi G(r/a, 0, 0), \quad (\text{C1})$$

where Green's function

$$G(\mathbf{R}) = \frac{1}{(2\pi)^3} \int_{-\pi}^{\pi} d^3k \frac{\prod_{j=1}^3 \cos(k_j R_j)}{4 \sum_{j=1}^3 \sin^2(k_j/2)} \quad (\text{C2})$$

can be computed in an efficient way via a recursion relation [50,62].

For the HYP2 static action [59–61], which was used for the computations on ensemble A^{HYP2} , the numerator of the integrand differs from Eq. (C2) by an additional factor,

from the lattice data points [see Sec. V, in particular Eq. (11)], where $G^e(r/a) = 4\pi G(r/a, 0, 0)$ for $e = A, B, C, D$, and $G^e(r/a) = 4\pi G^{\text{HYP}}(r/a, 0, 0)$ for $e = A^{\text{HYP2}}$. α' is proportional to the strong coupling and is determined by a fit to the lattice data (see again Sec. V). Similarly, we subtract $\Delta V_{\text{hybrid}}^{\text{lat},e}(r) = -(1/8)\Delta V_{\Sigma_g^+}^{\text{lat},e}(r)$ from the lattice data points for the Π_u and Σ_u^- hybrid static

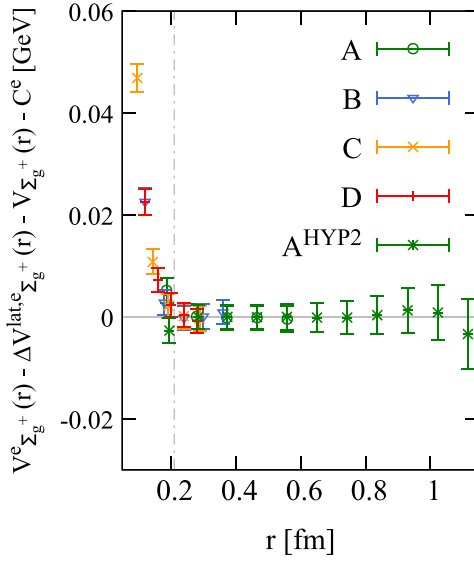


FIG. 7. Comparison of unimproved (left) and improved (right) lattice data points for the Σ_g^+ static potential from our five ensembles A, B, C, D, and A^{HYP2} . We subtract $V_{\Sigma_g^+}(r) + C^e$ with $V_{\Sigma_g^+}(r)$ defined in Eq. (9) and parameters obtained by a fit to data points with $r \geq 0.2$ fm (indicated by the vertical dashed line) as listed in Table IV.

potentials, which are repulsive and, in leading-order perturbation theory, suppressed by the factor $1/8$ relative to the ordinary static potential.

The benefit of applying tree-level improvement when combining lattice field theory results obtained at different lattice spacings and with different static actions is demonstrated in Fig. 7, where we compare unimproved and improved data points for the Σ_g^+ potential from our five ensembles. The two plots show that the majority of improved data points are consistent with a single curve, while unimproved data points from different ensembles exhibit strong discrepancies for $r \lesssim 0.4$ fm.

TABLE VIII. Bare lattice data points for the Σ_g^+ , Π_u , and Σ_u^- static potentials in units of the lattice spacing (see Sec. IV).

Ensemble	r/a	$V_{\Sigma_g^+}^e a$	$V_{\Pi_u}^e a$	$V_{\Sigma_u^-}^e a$
A	2	0.596753(62)	1.2527(28)	1.2813(35)
	3	0.699138(134)	1.2457(27)	1.2972(41)
	4	0.772857(238)	1.2476(27)	1.3228(48)
	5	0.835109(387)	1.2570(28)	1.3547(58)
	6	0.891807(601)	1.2726(30)	1.3898(71)
	B	2	0.512961(19)	1.0067(46)
3		0.584400(40)	0.9996(45)	1.0155(56)
4		0.629977(73)	0.9966(44)	1.0212(61)
5		0.664972(117)	0.9963(43)	1.0315(67)
6		0.694703(175)	0.9973(82)	1.0432(76)
C		2	0.478535(11)	0.9091(40)
	3	0.540198(26)	0.9019(39)	0.9095(25)
	4	0.577592(47)	0.8976(37)	0.9110(25)
	5	0.604988(76)	0.8959(21)	0.9154(26)
	6	0.627360(111)	0.8954(20)	0.9210(28)
	D	2	0.453884(7)	0.8417(22)
3		0.509466(16)	0.8353(21)	0.8396(23)
4		0.542058(29)	0.8317(21)	0.8393(23)
5		0.565146(46)	0.8295(20)	0.8412(24)
6		0.583422(68)	0.8282(19)	0.8438(25)
7		0.598894(93)	0.8276(19)	0.8479(26)
A ^{HYP2}		2	0.116648(13)	0.7427(21)
	3	0.206462(31)	0.7369(18)	0.7901(8)
	4	0.275767(60)	0.7395(17)	0.8151(9)
	5	0.336546(114)	0.7483(18)	0.8469(10)
	6	0.392896(184)	0.7621(19)	0.8809(6)
	7	0.446512(289)	0.7805(21)	0.9171(7)
	8	0.498474(446)	0.8037(24)	0.9586(8)
	9	0.549517(680)	0.8326(15)	0.9966(9)
	10	0.599980(1032)	0.8613(19)	1.0382(11)
	11	0.649218(1563)	0.8920(23)	1.0831(13)
	12	0.696191(2361)	0.9243(28)	1.1266(15)

APPENDIX D: SUMMARY OF SU(3) LATTICE FIELD THEORY RESULTS FOR THE Σ_g^+ , Π_u , AND Σ_u^- STATIC POTENTIALS

In Table VIII we list $V_{\Lambda_\eta}^e(r)a$, the bare lattice data points in units of the lattice spacing (see Sec. IV). In Table IX we list $\tilde{V}_{\Lambda_\eta}^e(r)$, the lattice data points defined in Eqs. (11) and (19), where the self-energy as well as lattice discretization errors at tree level and proportional to a^2 are removed.

TABLE IX. Lattice data points defined in Eqs. (11) and (19), where the self-energy as well as lattice discretization errors at tree level and proportional to a^2 are removed (using Fit 1), for the Σ_g^+ , Π_u , and Σ_u^- static potentials in units of GeV (physical units are introduced by setting $r_0 = 0.5$ fm).

Ensemble	r/a	r [fm]	$\tilde{V}_{\Sigma_g^+}^e$ [GeV]	$\tilde{V}_{\Pi_u}^e$ [GeV]	$\tilde{V}_{\Sigma_u^-}^e$ [GeV]
A	2	0.1863	-0.1033(24)	1.2245(73)	1.2541(76)
	3	0.2794	0.0929(24)	1.2122(76)	1.2903(91)
	4	0.3726	0.2428(24)	1.2169(78)	1.3454(108)
	5	0.4657	0.3726(24)	1.2372(81)	1.4131(127)
	6	0.5589	0.4919(25)	1.2703(84)	1.4876(154)
	B	2	0.1201	-0.3254(26)	1.2318(150)
3		0.1801	-0.1227(24)	1.2127(149)	1.2521(183)
4		0.2402	0.0174(24)	1.2039(147)	1.2719(199)
5		0.3002	0.1292(24)	1.2035(147)	1.3061(220)
6		0.3603	0.2256(24)	1.2067(270)	1.3449(246)
C		2	0.0960	-0.4459(28)	1.2489(168)
	3	0.1441	-0.2326(24)	1.2241(165)	1.2472(108)
	4	0.1921	-0.0910(24)	1.2082(159)	1.2551(112)
	5	0.2401	0.0176(24)	1.2015(95)	1.2737(116)
	6	0.2881	0.1079(24)	1.1999(93)	1.2968(122)
	D	2	0.0800	-0.5520(30)	1.2754(108)
3		0.1200	-0.3260(25)	1.2497(109)	1.2653(116)
4		0.1600	-0.1796(24)	1.2337(106)	1.2655(118)
5		0.2000	-0.0706(24)	1.2234(104)	1.2753(122)
6		0.2400	0.0176(24)	1.2173(101)	1.2888(127)
7		0.2800	0.0930(24)	1.2148(99)	1.3088(133)
A ^{HYP2}		2	0.1863	-0.1112(24)	1.2267(58)
	3	0.2794	0.0928(23)	1.2126(56)	1.2904(51)
	4	0.3726	0.2430(24)	1.2178(58)	1.3430(53)
	5	0.4657	0.3727(24)	1.2364(61)	1.4102(54)
	6	0.5589	0.4923(26)	1.2654(66)	1.4822(52)
	7	0.6520	0.6059(28)	1.3045(72)	1.5588(52)
	8	0.7452	0.7159(32)	1.3538(79)	1.6467(53)
	9	0.8383	0.8240(37)	1.4148(74)	1.7273(54)
	10	0.9315	0.9308(44)	1.4757(79)	1.8153(55)
	11	1.0246	1.0351(54)	1.5407(85)	1.9104(58)
	12	1.1178	1.1345(69)	1.6090(91)	2.0026(61)

TABLE X. Gauge link ensembles for gauge group SU(2).

Ensemble	β	a in fm [56]	$(L/a)^3 \times T/a$	N_{sim}	N_{total}	N_{or}	N_{therm}	N_{sep}	N_{meas}
a	2.50	0.078	$16^3 \times 16$	20	40000	0	10000	100	6000
b	2.70	0.041	$32^3 \times 32$	20	25000	0	10000	100	3000
c	2.85	0.026	$48^3 \times 48$	20	25000	0	10000	200	1500

APPENDIX E: SU(2) LATTICE FIELD THEORY RESULTS FOR THE Σ_g^+ , Π_u , AND Σ_u^- STATIC POTENTIALS

We carried out computations for gauge group SU(2) analogous to those for gauge group SU(3) discussed and presented in the main sections of this work. We generated three ensembles of gauge link configurations with gauge couplings $\beta = 2.85, 2.70, 2.50$. We relate the lattice spacing a to the scale t_0 using a parametrization of $\ln(t_0/a^2)$ determined in Ref. [56] via the gradient flow. Physical units are then introduced by setting $\sqrt{8t_0} = 0.3010$ fm, which

corresponds to $r_0 = 0.5$ fm. The details of the gauge link ensembles are summarized in Table X. The three lattice volumes are quite similar, $L^3 \times T \approx (1.3 \text{ fm})^3 \times (1.3 \text{ fm})$. For the investigation of finite volume effects in Sec. VI B, additional ensembles with both smaller and larger lattice volumes at gauge couplings $\beta = 3.00, 2.85, 2.70, 2.50$ were generated.

In Table XI we list $V_{\Lambda_\eta^c}^e(r)a$, the bare lattice data points in units of the lattice spacing. These can be used to generate parametrizations, using methods as e.g. discussed in Sec. V.

TABLE XI. Bare lattice data points for the Σ_g^+ , Π_u , and Σ_u^- static potentials in units of the lattice spacing (see Table X) for gauge group SU(2).

Ensemble	r/a	$V_{\Sigma_g^+}^e a$	$V_{\Pi_u}^e a$	$V_{\Sigma_u^-}^e a$
a	2	0.484308(68)	1.1150(47)	1.1448(58)
	3	0.565442(151)	1.0899(42)	1.1428(61)
	4	0.623418(271)	1.0803(38)	1.1486(66)
	5	0.671506(422)	1.0792(39)	1.1677(74)
	6	0.714737(645)	1.0819(39)	1.1864(86)
	7	0.755318(914)	1.0901(43)	1.2149(98)
	8	0.794584(1292)	1.1012(46)	1.2307(115)
	b	2	0.395714(7)	0.8213(18)
3		0.446300(17)	0.8040(29)	0.8144(20)
4		0.476883(31)	0.7964(16)	0.8104(20)
5		0.499216(50)	0.7903(16)	0.8101(21)
6		0.517411(74)	0.7860(16)	0.8118(22)
7		0.533191(104)	0.7832(15)	0.8153(23)
8		0.547435(138)	0.7817(15)	0.8198(24)
9		0.560630(177)	0.7807(15)	0.8254(25)
10		0.573101(223)	0.7812(15)	0.8314(27)
c		2	0.353848(16)	0.6860(25)
	3	0.394722(30)	0.6734(23)	0.6737(23)
	4	0.417829(50)	0.6646(22)	0.6680(21)
	5	0.433611(87)	0.6609(22)	0.6654(22)
	6	0.445685(89)	0.6567(19)	0.6643(22)
	7	0.455557(110)	0.6524(19)	0.6644(22)
	8	0.463982(141)	0.6503(18)	0.6643(23)
	9	0.471474(164)	0.6493(19)	0.6635(25)
	10	0.478364(214)	0.6458(18)	0.6648(26)
	11	0.484684(228)	0.6438(19)	0.6662(27)

- [1] S. L. Olsen, T. Skwarnicki, and D. Zieminska, Nonstandard heavy mesons and baryons: Experimental evidence, *Rev. Mod. Phys.* **90**, 015003 (2018).
- [2] E. Braaten, C. Langmack, and D. H. Smith, Selection Rules for Hadronic Transitions of XYZ Mesons, *Phys. Rev. Lett.* **112**, 222001 (2014).
- [3] C. Meyer and E. Swanson, Hybrid mesons, *Prog. Part. Nucl. Phys.* **82**, 21 (2015).
- [4] E. S. Swanson, XYZ states: Theory overview, *AIP Conf. Proc.* **1735**, 020013 (2016).
- [5] R. F. Lebed, R. E. Mitchell, and E. S. Swanson, Heavy-quark QCD exotica, *Prog. Part. Nucl. Phys.* **93**, 143 (2017).
- [6] N. Brambilla, S. Eidelman, C. Hanhart, A. Nefediev, C.-P. Shen, C. E. Thomas, A. Vairo, and C.-Z. Yuan, The XYZ states: Experimental and theoretical status and perspectives, *Phys. Rep.* **873**, 1 (2020).
- [7] S. Perantonis and C. Michael, Static potentials and hybrid mesons from pure SU(3) lattice gauge theory, *Nucl. Phys.* **B347**, 854 (1990).
- [8] K. Juge, J. Kuti, and C. Morningstar, Gluon excitations of the static quark potential and the hybrid quarkonium spectrum, *Nucl. Phys. B Proc. Suppl.* **63**, 326 (1998).
- [9] K. J. Juge, J. Kuti, and C. J. Morningstar, *Ab Initio* Study of Hybrid $\bar{b}gb$ Mesons, *Phys. Rev. Lett.* **82**, 4400 (1999).
- [10] P. Guo, A. P. Szczepaniak, G. Galata, A. Vassallo, and E. Santopinto, Heavy quarkonium hybrids from Coulomb gauge QCD, *Phys. Rev. D* **78**, 056003 (2008).
- [11] E. Braaten, C. Langmack, and D. H. Smith, Born-Oppenheimer approximation for the XYZ mesons, *Phys. Rev. D* **90**, 014044 (2014).
- [12] M. Berwein, N. Brambilla, J. Tarrús Castellà, and A. Vairo, Quarkonium hybrids with nonrelativistic effective field theories, *Phys. Rev. D* **92**, 114019 (2015).
- [13] R. Onocala and J. Soto, Heavy quarkonium hybrids: Spectrum, decay and mixing, *Phys. Rev. D* **96**, 014004 (2017).
- [14] S. Capitani, O. Philipsen, C. Reisinger, C. Riehl, and M. Wagner, Precision computation of hybrid static potentials in SU(3) lattice gauge theory, *Phys. Rev. D* **99**, 034502 (2019).
- [15] N. Brambilla, W. K. Lai, J. Segovia, J. Tarrús Castellà, and A. Vairo, Spin structure of heavy-quark hybrids, *Phys. Rev. D* **99**, 014017 (2019); Erratum, *Phys. Rev. D* **101**, 099902(E) (2020).
- [16] N. Brambilla, W. K. Lai, J. Segovia, and J. Tarrús Castellà, QCD spin effects in the heavy hybrid potentials and spectra, *Phys. Rev. D* **101**, 054040 (2020).
- [17] C. Bernard, T. Burch, E. B. Gregory, D. Toussaint, C. E. DeTar, J. Osborn, S. A. Gottlieb, U. M. Heller, and R. Sugar, Lattice calculation of $1 - +$ hybrid mesons with improved Kogut-Susskind fermions, *Phys. Rev. D* **68**, 074505 (2003).
- [18] G. S. Bali, S. Collins, and C. Ehmman, Charmonium spectroscopy and mixing with light quark and open charm states from $n_F = 2$ lattice QCD, *Phys. Rev. D* **84**, 094506 (2011).
- [19] G. K. C. Cheung, C. O'Hara, G. Moir, M. Peardon, S. M. Ryan, C. E. Thomas, and D. Tims (Hadron Spectrum Collaboration), Excited and exotic charmonium, D_s and D meson spectra for two light quark masses from lattice QCD, *J. High Energy Phys.* **12** (2016) 089.
- [20] G. Ray and C. McNeile, Determination of hybrid charmonium meson masses, [arXiv:2110.14101](https://arxiv.org/abs/2110.14101).
- [21] M. Born and R. Oppenheimer, Zur Quantentheorie der Molekeln, *Ann. Phys. (Berlin)* **389**, 457 (1927).
- [22] N. Brambilla, G. a. Krein, J. Tarrús Castellà, and A. Vairo, Born-Oppenheimer approximation in an effective field theory language, *Phys. Rev. D* **97**, 016016 (2018).
- [23] L. A. Griffiths, C. Michael, and P. E. L. Rakow, Mesons with excited glue, *Phys. Lett.* **129B**, 351 (1983).
- [24] N. A. Campbell, L. A. Griffiths, C. Michael, and P. E. L. Rakow, Mesons with excited glue from SU(3) lattice gauge theory, *Phys. Lett.* **142B**, 291 (1984).
- [25] N. A. Campbell, A. Huntley, and C. Michael, Heavy quark potentials and hybrid mesons from SU(3) lattice gauge theory, *Nucl. Phys.* **B306**, 51 (1988).
- [26] S. Perantonis, A. Huntley, and C. Michael, Static potentials from pure SU(2) lattice gauge theory, *Nucl. Phys.* **326**, 544 (1989).
- [27] C. Michael and S. J. Perantonis, Potentials and glueballs at large beta in SU(2) pure gauge theory, *J. Phys. G* **18**, 1725 (1992).
- [28] M. J. Peardon, Coarse lattice results for glueballs and hybrids, *Nucl. Phys. B Proc. Suppl.* **63**, 22 (1998).
- [29] K. J. Juge, J. Kuti, and C. J. Morningstar, A study of hybrid quarkonium using lattice QCD, *AIP Conf. Proc.* **432**, 136 (1998).
- [30] C. Morningstar, K. J. Juge, and J. Kuti, Gluon excitations of the static quark potential, [arXiv:hep-lat/9809015](https://arxiv.org/abs/hep-lat/9809015).
- [31] C. Michael, Hadronic spectroscopy from the lattice: Glueballs and hybrid mesons, *Nucl. Phys.* **A655**, c12 (1999).
- [32] C. Michael, Quarkonia and hybrids from the lattice, *Proc. Sci.* **8** (1999) 001 [[arXiv:hep-ph/9911219](https://arxiv.org/abs/hep-ph/9911219)].
- [33] K. J. Juge, J. Kuti, and C. J. Morningstar, The heavy hybrid spectrum from NRQCD and the Born-Oppenheimer approximation, *Nucl. Phys. B, Proc. Suppl.* **83**, 304 (2000).
- [34] G. S. Bali, B. Bolder, N. Eicker, T. Lippert, B. Orth, P. Ueberholz, K. Schilling, and T. Struckmann (SESAM and T χ L Collaborations), Static potentials and glueball masses from QCD simulations with Wilson sea quarks, *Phys. Rev. D* **62**, 054503 (2000).
- [35] C. Morningstar, Gluonic excitations in lattice QCD: A brief survey, *AIP Conf. Proc.* **619**, 231 (2002).
- [36] K. J. Juge, J. Kuti, and C. Morningstar, Fine Structure of the QCD String Spectrum, *Phys. Rev. Lett.* **90**, 161601 (2003).
- [37] K. J. Juge, J. Kuti, and C. Morningstar, The heavy quark hybrid meson spectrum in lattice QCD, *AIP Conf. Proc.* **688**, 193 (2003).
- [38] C. Michael, Exotics, *Int. Rev. Nucl. Phys.* **9**, 103 (2004).
- [39] C. Michael, Hybrid mesons from the lattice, [arXiv:hep-ph/0308293](https://arxiv.org/abs/hep-ph/0308293).
- [40] G. S. Bali and A. Pineda, QCD phenomenology of static sources and gluonic excitations at short distances, *Phys. Rev. D* **69**, 094001 (2004).
- [41] K. J. Juge, J. Kuti, and C. Morningstar, Excitations of the static quark anti-quark system in several gauge theories, [arXiv:hep-lat/0312019](https://arxiv.org/abs/hep-lat/0312019).
- [42] P. Wolf and M. Wagner, Lattice study of hybrid static potentials, *J. Phys. Conf. Ser.* **599**, 012005 (2015).
- [43] C. Reisinger, S. Capitani, O. Philipsen, and M. Wagner, Computation of hybrid static potentials in SU(3) lattice gauge theory, *EPJ Web Conf.* **175**, 05012 (2018).

- [44] P. Bicudo, M. Cardoso, and N. Cardoso, Colour fields of the quark-antiquark excited flux tube, *EPJ Web Conf.* **175**, 14009 (2018).
- [45] P. Bicudo, N. Cardoso, and M. Cardoso, Color field densities of the quark-antiquark excited flux tubes in SU(3) lattice QCD, *Phys. Rev. D* **98**, 114507 (2018).
- [46] C. Reisinger, S. Capitani, L. Müller, O. Philipsen, and M. Wagner, Computation of hybrid static potentials from optimized trial states in SU(3) lattice gauge theory, *Proc. Sci. LATTICE2018* (2018) 054 [arXiv:1810.13284].
- [47] M. Lüscher and P. Weisz, Locality and exponential error reduction in numerical lattice gauge theory, *J. High Energy Phys.* **09** (2001) 010.
- [48] K. Jansen, C. Michael, A. Shindler, and M. Wagner (ETM Collaboration), The Static-light meson spectrum from twisted mass lattice QCD, *J. High Energy Phys.* **12** (2008) 058.
- [49] O. Philipsen, C. Pinke, A. Sciarra, and M. Bach, CL²QCD—Lattice QCD based on OpenCL, *Proc. Sci. LATTICE2014* (2014) 038 [arXiv:1411.5219].
- [50] S. Necco and R. Sommer, The $N(f) = 0$ heavy quark potential from short to intermediate distances, *Nucl. Phys.* **B622**, 328 (2002).
- [51] R. Sommer, Scale setting in lattice QCD, *Proc. Sci. LATTICE2013* (2014) 015 [arXiv:1401.3270].
- [52] N. Brambilla, V. Leino, O. Philipsen, C. Reisinger, A. Vairo, and M. Wagner, Lattice gauge theory computation of the static force, arXiv:2106.01794.
- [53] M. Guagnelli, R. Sommer, and H. Wittig (ALPHA Collaboration), Precision computation of a low-energy reference scale in quenched lattice QCD, *Nucl. Phys.* **B535**, 389 (1998).
- [54] A. Hasenfratz, R. Hoffmann, and F. Knechtli, The static potential with hypercubic blocking, *Nucl. Phys. B Proc. Suppl.* **106**, 418 (2002).
- [55] K. Jansen, F. Karbstein, A. Nagy, and M. Wagner (ETM Collaboration), $\Lambda_{\overline{MS}}^{(n_f=2)}$ from the static potential for QCD with $n_f = 2$ dynamical quark flavors, *J. High Energy Phys.* **01** (2012) 025.
- [56] T. Hirakida, E. Itou, and H. Kouno, Thermodynamics for pure SU(2) gauge theory using gradient flow, *Prog. Theor. Exp. Phys.* **2019**, 033B01 (2019).
- [57] N. Brambilla, A. Pineda, J. Soto, and A. Vairo, Potential NRQCD: An effective theory for heavy quarkonium, *Nucl. Phys.* **B566**, 275 (2000).
- [58] J. Soto, Heavy quarkonium hybrids, *Nucl. Part. Phys. Proc.* **294–296**, 87 (2018).
- [59] M. Della Morte, A. Shindler, and R. Sommer, On lattice actions for static quarks, *J. High Energy Phys.* **08** (2005) 051.
- [60] A. Hasenfratz and F. Knechtli, Flavor symmetry and the static potential with hypercubic blocking, *Phys. Rev. D* **64**, 034504 (2001).
- [61] M. Della Morte, S. Durr, J. Heitger, H. Molke, J. Rolf, A. Shindler, and R. Sommer (ALPHA Collaboration), Lattice HQET with exponentially improved statistical precision, *Phys. Lett. B* **581**, 93 (2004); Erratum, *Phys. Lett.* **B612**, 313(E) (2005).
- [62] M. Lüscher and P. Weisz, Coordinate space methods for the evaluation of Feynman diagrams in lattice field theories, *Nucl. Phys.* **B445**, 429 (1995).
- [63] F. Karbstein, M. Wagner, and M. Weber, Determination of $\Lambda_{\overline{MS}}^{(n_f=2)}$ and analytic parametrization of the static quark-antiquark potential, *Phys. Rev. D* **98**, 114506 (2018).
- [64] Y. Koma, M. Koma, and H. Wittig, Relativistic corrections to the static potential at $O(1/m)$ and $O(1/m^{**2})$, *Proc. Sci. LATTICE2007* (2007) 111 [arXiv:0711.2322].
- [65] A. Vairo, Quarkonia: A theoretical frame, arXiv:0912.4422.
- [66] S. Godfrey and N. Isgur, Mesons in a relativized quark model with chromodynamics, *Phys. Rev. D* **32**, 189 (1985).
- [67] M. Tanabashi *et al.* (Particle Data Group Collaboration), Review of particle physics, *Phys. Rev. D* **98**, 030001 (2018).
- [68] S. Schaefer, R. Sommer, and F. Virota (ALPHA Collaboration), Critical slowing down and error analysis in lattice QCD simulations, *Nucl. Phys.* **B845**, 93 (2011).
- [69] R. Brower, S. Chandrasekharan, J. W. Negele, and U. Wiese, QCD at fixed topology, *Phys. Lett. B* **560**, 64 (2003).
- [70] S. Aoki, H. Fukaya, S. Hashimoto, and T. Onogi, Finite volume QCD at fixed topological charge, *Phys. Rev. D* **76**, 054508 (2007).
- [71] A. Dromard and M. Wagner, Extracting hadron masses from fixed topology simulations, *Phys. Rev. D* **90**, 074505 (2014).
- [72] W. Bietenholz, C. Czaban, A. Dromard, U. Gerber, C. P. Hofmann, H. Mejía-Díaz, and M. Wagner, Interpreting numerical measurements in fixed topological sectors, *Phys. Rev. D* **93**, 114516 (2016).
- [73] K. Cichy, A. Dromard, E. Garcia-Ramos, K. Ottnad, C. Urbach, M. Wagner, U. Wenger, and F. Zimmermann, Comparison of different lattice definitions of the topological charge, *Proc. Sci. LATTICE2014* (2014) 075 [arXiv:1411.1205].
- [74] C. Alexandrou, A. Athenodorou, K. Cichy, A. Dromard, E. Garcia-Ramos, K. Jansen, U. Wenger, and F. Zimmermann, Comparison of topological charge definitions in Lattice QCD, *Eur. Phys. J. C* **80**, 424 (2020).
- [75] A. Athenodorou and M. Teper, SU(N) gauge theories in 3 + 1 dimensions: Glueball spectrum, string tensions and topology, *J. High Energy Phys.* **12** (2021) 082.
- [76] M. Lüscher, Volume dependence of the energy spectrum in massive quantum field theories. 1. Stable particle states, *Commun. Math. Phys.* **104**, 177 (1986).
- [77] M. Fukugita, H. Mino, M. Okawa, G. Parisi, and A. Ukawa, Finite size effect for hadron masses in lattice QCD, *Phys. Lett. B* **294**, 380 (1992).
- [78] L. Müller, O. Philipsen, C. Reisinger, and M. Wagner, Hybrid static potential flux tubes from SU(2) and SU(3) lattice gauge theory, *Phys. Rev. D* **100**, 054503 (2019).
- [79] C. J. Morningstar and M. J. Peardon, The glueball spectrum from an anisotropic lattice study, *Phys. Rev. D* **60**, 034509 (1999).